

## Crystal-Chemical Origins of the Ultrahigh Conductivity of Metallic Delafossites

Yi Zhang (張易)<sup>1</sup>, Fred Tutt<sup>1</sup>, Guy N. Evans<sup>2</sup>, Prachi Sharma<sup>1,3</sup>, Greg Haugstad<sup>4</sup>, Ben Kaiser<sup>1</sup>, Justin Ramberger<sup>1</sup>, Samuel Bayliff<sup>3</sup>, Yu Tao<sup>1</sup>, Mike Manno<sup>1</sup>, Javier Garcia-Barriocanal<sup>4</sup>, Rafael M. Fernandes<sup>3</sup>, Turan Birol<sup>1</sup>, William E. Seyfried Jr.<sup>2</sup>, and Chris Leighton<sup>1\*</sup>

<sup>1</sup>*Department of Chemical Engineering and Materials Science, University of Minnesota, Minneapolis, MN 55455, USA*

<sup>2</sup>*Department of Earth and Environmental Sciences, University of Minnesota, Minneapolis, MN 55455, USA*

<sup>3</sup>*School of Physics and Astronomy, University of Minnesota, Minneapolis, MN 55455, USA*

<sup>4</sup>*Characterization Facility, University of Minnesota, Minneapolis, MN 55455, USA*

**ABSTRACT:** Despite their highly anisotropic complex-oxidic nature, certain delafossite compounds (*e.g.*, PdCoO<sub>2</sub>) are the most conductive oxides known, for reasons that remain poorly understood. It is widely accepted that these materials are somehow ultrapure, although the methods for their growth (which produce only small crystals) are not typically capable of such. Here, we report a new approach to PdCoO<sub>2</sub> crystal growth, using chemical vapor transport to achieve order-of-magnitude gains in size, the highest structural qualities reported, and record residual resistivity ratios (>440). Nevertheless, the first detailed mass spectrometry on these materials reveals that they are *not* ultrapure, typically harboring 100s-of-parts-per-million impurity levels. For crystal-chemical reasons that we elaborate in full, however, the majority of these impurities must reside in Co-O octahedral layers, leaving the conductive Pd sheets highly pure (~1 ppm). We thus conclude that a “sublattice purification” mechanism is essential to the ultrahigh low-temperature conductivity and mean-free-path of metallic delafossites.

\*Corresponding author: [leighton@umn.edu](mailto:leighton@umn.edu)

## INTRODUCTION

Complex oxide materials have proven to be fertile ground for the discovery of new physical phenomena and the advancement of technologically important device function, the  $ABO_3$  perovskites being a prime example (1–4). Many related classes of complex oxides offer similarly substantial potential but remain less extensively studied.  $ABO_2$  delafossites are one example, where two-dimensional triangular sheets of typically monovalent A ions are separated by layers of edge-shared  $BO_6$  octahedra (5–10). Most delafossite compounds are insulating or semiconducting, such as the  $CuFeO_2$  studied for frustrated magnetism (11, 12) and the  $CuAlO_2$  considered for transparent conductive oxide applications (13). It has been known since 1971, however (5–8), that some delafossites exhibit metallic character, as exemplified by  $PdCoO_2$  and  $PtCoO_2$ . These metallic delafossites received little attention until the relatively recent discovery that, in bulk-single-crystal form, *they are the most conductive oxides known* (5, 10). While their  $c$ -axis resistivities ( $\rho_c$ ) are more than 100 times higher (5, 8, 9, 14–16), the room-temperature  $a$ - $b$ -plane resistivities ( $\rho_{ab}$ ) of  $PdCoO_2$  and  $PtCoO_2$  are only 3.1 and 1.8  $\mu\Omega\text{cm}$ , respectively (17), comparable to or lower than Au (5). Their low-temperature ( $T$ ) residual  $\rho_{ab}$  values fall as low as 8.1  $\text{n}\Omega\text{cm}$  (17), implying residual resistivity ratios (RRRs) up to 376 (17) and low- $T$  mean-free-paths of  $\sim 20$   $\mu\text{m}$  (5, 15). These are astonishing values, particularly in complex oxides, in such highly anisotropic structures, and given the relatively little materials development performed on these systems.

The electronic structure of metallic delafossites is similarly noteworthy. Taking  $PdCoO_2$  as an example, the established  $R-3m$  structure of the  $3R$  polymorph (5–7, 9, 10, 18) results in a strikingly simple electronic structure where a single Pd  $d$  band crosses the Fermi level, with only modest

contributions from Co, and negligible O character (5, 9, 10, 18–21). The triangular Pd<sup>1+</sup> planes thus generate a Fermi surface closely approximating a hexagonal-cross-section cylinder filling half the hexagonal Brillouin zone in the  $a^*$ - $b^*$  reciprocal-space plane (5, 15, 18–23). The remarkable simplicity of this electronic structure is underscored by electron effective masses of only 1-1.7  $m_e$  (5, 15, 18, 24). The edge-shared CoO<sub>6</sub> octahedra also have short Co-O bond lengths and large crystal field splitting, stabilizing low-spin ( $S = 0$ ) Co<sup>3+</sup> (18). PdCoO<sub>2</sub> is thus a model metallic delafossite, which can be thought of as triangular metallic sheets of Pd<sup>1+</sup> separated by insulating nonmagnetic layers of Co<sup>3+</sup>O<sub>6</sub> edge-shared octahedra.

The above attributes, particularly the exceptional low- $T$  mean-free-path and simple hexagonal Fermi surface, have enabled a remarkable string of recent achievements with bulk crystals of PtCoO<sub>2</sub> and PdCoO<sub>2</sub>. These include observations of: various types of quantum oscillations (14, 15, 25, 26), very large positive magnetoresistance along the  $c$ -axis (27), potential phonon-drag effects in resistivity (15), possible hydrodynamic electron transport (25), and itinerant surface ferromagnetism (23, 28, 29). Yet more recently, non-local electrodynamics (30), directional ballistic transport (31), supergeometric electron focusing (32), and non-local transport (33) have been reported in PdCoO<sub>2</sub> crystals and micron-scale structures, exploiting the long mean-free-path and anisotropic two-dimensional Fermi surface. The addition of magnetic moments in PdCrO<sub>2</sub> adds further richness, encompassing magnetic frustration (34–36), a complex antiferromagnetic spin structure (34–37), potential chirality (37), an anomalous Hall effect (38, 39), and  $T$ -linear resistivity (40, 41) potentially due to magneto-elastic scattering (41). Metallic delafossites are thus making their mark in condensed matter and materials physics, and potential applications are already being explored, in nanoelectronic interconnects (42), harsh-environment electronic devices (43–45), electrocatalysis (43, 46), ballistic transport devices (31–33, 43, 44), *etc.*

Despite this progress, the *origins* of the ultrahigh conductivities and mean-free-paths in metallic delafossites remain unclear. While progress has been made with understanding thermal properties of PdCoO<sub>2</sub> (18) and related phonon spectra (47, 48), much remains to be elucidated regarding electron-phonon scattering and coupling (5, 14) and thus the low room-*T* resistivities (5). Yet more urgently given the above advances (14, 15, 25–27, 29–33), the origin of the outstanding *a-b*-plane residual resistivities and low-*T* mean-free-paths remain incompletely understood (5, 43). It is widely accepted that ultrahigh purity and ultralow defect density are necessary for such behavior (5, 14, 15, 25, 49, 50), but, confusingly, the crystal growth methods typically applied to metallic delafossites (6, 14, 16, 51–54) are not generally capable of such (5, 49). The prevailing method for PdCoO<sub>2</sub> and PtCoO<sub>2</sub> is a metathesis-based flux growth (6, 14, 16, 52, 53), which is not well understood, is typically limited to ~1-mm lateral sizes, and is not performed under conditions that would be expected to realize ultrahigh purity. Multiple authors have commented on the crude synthesis methods for metallic delafossites relative to other systems with comparable mean-free-paths (5, 49). On the other hand, recent electron microscopy on single-crystal PdCoO<sub>2</sub> supports sufficiently low defect densities that only upper limits could be placed (49, 55). An electronic transport study of several metallic delafossites as a function of irradiation-induced point defect density also evidenced extraordinarily low initial defect densities on the Pd/Pt planes, insensitive to the (unknown) disorder level on the B-O layers (49). It is thus unclear what the impurity and defect densities actually are in single-crystal metallic delafossites, how they are divided between A and B-O planes (49), if/how defect densities are minimized by current growth methods (49), or whether some form of defect mitigation or tolerance occurs (49). One proposal for the latter is the hidden kagome picture recently advanced to explain reduced electron-impurity scattering (56).

The current work seeks to elucidate some of the above through advances that are thus far absent from the PdCoO<sub>2</sub> literature: improvements in bulk crystal growth in terms of mechanistic understanding, crystal size, defect density, and purity; more extensive structural and chemical characterization; and comprehensive trace impurity analysis. The latter is particularly conspicuous in its absence from the metallic delafossite literature, likely because the premier method – inductively coupled plasma mass spectrometry (ICP-MS) – typically involves acid digestion. Metallic delafossites such as PdCoO<sub>2</sub> and PtCoO<sub>2</sub> are unusually stable in extreme pH, however (43–45), likely hindering prior attempts at comprehensive trace impurity analysis.

Here, we first elaborate on a new crystal growth method for PdCoO<sub>2</sub> based on chemical vapor transport (CVT), for which a simple mechanism is proposed. CVT is then compared to the established metathesis/flux method and is shown to enable orders-of-magnitude gains in crystal size and mass, the highest structural quality yet reported, and record RRR. Nevertheless, particle-induced X-ray emission (PIXE) and low-*T* magnetometry suggest significant impurity concentrations. Enabled by microwave digestion methods, the first comprehensive trace impurity analyses of metathesis/flux-grown and CVT-grown PdCoO<sub>2</sub> crystals were thus performed by ICP-MS, with remarkable conclusions. Specifically, these metallic delafossite crystals are definitively *not* ultrapure in a general sense. Standard metathesis/flux crystals typically have ~250 ppm metals-basis impurities; CVT crystals are purer but still harbor ~50 ppm impurities. Through a detailed crystal-chemistry-based analysis, however, we show that the vast majority of these impurities must populate Co-O octahedral layers, while as few as four elements can conceivably substitute for Pd. The concentration of these elements is of order 1 ppm, ~100 times lower than the total impurity concentration, which is shown to be in quantitative agreement with the measured residual  $\rho_{\text{ab}}$ . We thus propose that a “sublattice purification” mechanism is central to the extraordinary low-*T*

conductivity of metallic delafossites, enabling ultrahigh purity in the conductive Pd/Pt sheets, largely unaffected by substantial impurity concentrations in the CoO<sub>6</sub> octahedra.

## RESULTS

### Chemical vapor transport crystal growth

As noted in the Introduction, metathesis-based flux growth has become standard for single-crystal PdCoO<sub>2</sub> and PtCoO<sub>2</sub> (6, 14, 16, 52, 53). This is based on metathesis reactions such as PdCl<sub>2</sub> + Pd + Co<sub>3</sub>O<sub>4</sub> → 2PdCoO<sub>2</sub> + CoCl<sub>2</sub>, *i.e.*, PdCl<sub>2</sub>, Pd, and Co<sub>3</sub>O<sub>4</sub> reagents (99.995-99.999% purity in our case) reacting to form the target PdCoO<sub>2</sub> plus a CoCl<sub>2</sub> by-product, which is chemically removed (see Methods for more details). In the current study, dwell temperatures of 700-750 °C were employed for metathesis growth, followed by cooling to 400 °C at 40-60 °C/h. As shown in the scanning electron microscopy (SEM) image in Fig. 1(b), the resulting product is a mass of PdCoO<sub>2</sub> crystals and crystallites. The optical microscope image in the inset to Fig. 1(b) highlights one of the largest crystals from a typical growth, measuring 0.8 × 0.6 mm<sup>2</sup> laterally, and 0.017 mm thick. This corresponds to 0.008 mm<sup>3</sup> and 0.065 mg, comparable to literature reports (16, 25, 31, 49, 50). Typical powder X-ray diffraction (PXRD) data from such crystals are shown in Fig. 1(d) (green), displaying a good match with a PdCoO<sub>2</sub> standard (grey), and yielding lattice parameters  $a = 2.8308 \pm 0.0002 \text{ \AA}$  and  $c = 17.747 \pm 0.002 \text{ \AA}$ , in agreement with accepted values (5, 6).

While such crystals have enabled exciting advances (14, 15, 17, 22–27, 29–33), as discussed in the Introduction, it is nevertheless true that little progress in PdCoO<sub>2</sub> crystal size or quality has been reported since *ca.* 2007. There is also limited understanding of the growth mechanism. Most publications describe the mechanism as “flux” or “self-flux” and employ specific temperature-time trajectories, but with little explicit justification (14, 16, 51–53). Seeking potential

improvement over this, we explored CVT crystal growth of PdCoO<sub>2</sub>. CVT is not commonly applied to complex oxides but the fact that PdCoO<sub>2</sub> decomposes (at ~800 °C in air, for example (45)) hints at CVT as a possibility, as does the relatively low decomposition temperature of PdCl<sub>2</sub> (~600 °C in low Cl<sub>2</sub> partial pressure (57, 58)), a potential transport agent. CVT was thus performed in a set-up shown schematically in Fig. 1(a), and elaborated upon in Methods and Supplementary Materials Sections A and B. The solid precursors are coarse PdCoO<sub>2</sub> powder derived from the above metathesis growth, along with 99.999%-pure PdCl<sub>2</sub>. At typical hot and cold zone temperatures of 760 and 710 °C, we propose that PdCl<sub>2</sub> decomposition is followed by a reaction such as  $\text{PdCoO}_2(\text{s}) + 2\text{Cl}_2(\text{g}) \leftrightarrow \text{PdCl}_2(\text{g}) + \text{CoCl}_2(\text{g}) + \text{O}_2(\text{g})$ , *i.e.*, Pd chloride and Co chloride vapor transport across the temperature gradient in a Cl<sub>2</sub>(g) and O<sub>2</sub>(g) atmosphere. The reaction runs to the left in the growth (cold) zone, resulting in PdCoO<sub>2</sub> crystals and chloride by-products, which are chemically removed (see Methods).

As shown in Fig. 1(c), after optimization of hot and cold zone temperatures, relatively large PdCoO<sub>2</sub> crystals and multicrystals derive from this process, at high yield (>90%). Specifically, the reaction product is a mix of single crystals and larger multicrystals, the latter likely forming due to nucleation of Pd or PdO seeds during the initial inverted-temperature-gradient period of the growth (see Methods and Supplementary Materials Section A). Multicrystals up to 12 × 12 mm<sup>2</sup> laterally and 0.3 mm thick are grown (Fig. 1(c)), corresponding to 43.2 mm<sup>3</sup> and 345 mg. Gently breaking apart such multicrystals isolates single crystals up to 6.0 × 4.0 mm<sup>2</sup> laterally and 0.17 mm thick, corresponding to 4.08 mm<sup>3</sup> and 32.6 mg. A representative example is shown in the inset to Fig. 1(c). These CVT PdCoO<sub>2</sub> multicrystals are thus larger than our metathesis/flux crystals by factors of ~15 in maximum lateral dimension, ~18 in thickness, and ~5300 in volume and mass.

Correspondingly, the CVT *single* crystals are larger than metathesis/flux single crystals by factors of ~8 in maximum lateral dimension, ~10 in thickness, and ~500 in volume and mass.

As illustrated in Fig. 1(e), PXRD patterns from powdered CVT crystals are also consistent with single-phase PdCoO<sub>2</sub>, with  $a = 2.8306 \pm 0.0002 \text{ \AA}$  and  $c = 17.746 \pm 0.002 \text{ \AA}$ . Intriguingly, large-scale comparisons of the lattice parameters for flux/metathesis and CVT crystals suggest subtle but significant differences. Averaged over all measured crystal batches, our metathesis flux crystals have  $a = 2.8309 \pm 0.0007 \text{ \AA}$ ,  $c = 17.749 \pm 0.005 \text{ \AA}$  (where the uncertainties are now standard deviations), while CVT crystals have  $a = 2.8302 \pm 0.0002 \text{ \AA}$ ,  $c = 17.745 \pm 0.002 \text{ \AA}$ . Both the lattice parameters and standard deviations are therefore lower in CVT crystals. The smaller standard deviation indicates better reproducibility with CVT, while decreased cell volume often indicates lower defect density (59–64), including in complex oxides (60–64). Minimization of unit cell volume has in fact emerged as a guiding principle for synthesis of highly perfect complex oxides with minimized densities of non-stoichiometry-accommodating defects (60–64). These data thus hint at lower defect densities in CVT-grown crystals, a conclusion that is reinforced below. As a final comment on structure, note that powdered samples of these CVT crystals were recently used in a 12-1000 K structural study *via* PXRD and accompanying refinement, confirming their single-phase nature and the thermal stability of the  $R\text{-}3m$  structure (18).

### **Structural and chemical characterization**

With CVT growth established to provide substantial improvements in PdCoO<sub>2</sub> crystal size and mass, and with improved defect density suggested by the lattice parameters, it is important to more rigorously assess structural quality and purity. Preliminary prior characterization established single crystallinity *via* two-dimensional single-crystal X-ray diffraction (18). In Fig. 2(a) this is improved

on by presenting Laue diffraction data conclusively confirming single crystallinity. The six-fold-symmetric pattern of diffraction spots down this [001] zone axis, interspersed with a second six-fold pattern of weaker spots (seen upon close examination of Fig. 2(a)), is as expected, as illustrated by the simulated pattern in Fig. 2(b) based on the accepted  $R\text{-}3m$  structure and lattice parameters (6). Wide-range specular high-resolution X-ray diffraction (HRXRD) was also performed on 001-oriented crystals (Fig. 2(c)), showing only sharp 003 through 0015 reflections, further confirming single crystallinity and phase purity. Of particular significance, a HRXRD rocking curve through the 006 reflection is shown in the inset to Fig. 2(c), revealing a full-width-at-half-maximum of only  $0.0089^\circ$ . To the best of our knowledge, this is the lowest rocking curve width reported for a metallic delafossite, demonstrating very low mosaic spread, another strong indicator of low defect density.

Turning to chemical characterization, Fig. 2(d) shows an energy-dispersive X-ray spectroscopy (EDS) scan from a representative  $\text{PdCoO}_2$  CVT crystal. Only Pd  $L$  and Co  $K$  peaks are clearly visible in this wide-energy-range scan, their relative intensities giving a Pd/Co ratio of  $0.98 \pm 0.05$ , consistent with the nominal stoichiometry. The inset to Fig. 2(d) focuses on the low-energy region shaded gray in the main panel, revealing, with the exception of a small detector-artifact peak and the inevitable C contamination in SEM/EDS, only peaks from Pd, Co, and O. Unsurprisingly, EDS is thus not sufficiently sensitive to detect any trace impurities in these  $\text{PdCoO}_2$  crystals, which was the motivation for the PIXE data in Fig. 2(e). PIXE is analogous to EDS except that the excitation is achieved with MeV-range He ions rather than electrons, vastly decreasing the broad background due to bremsstrahlung. As can be seen in Fig. 2(e), which shows spectra from two different CVT crystals (orange and blue), PIXE thus exposes a plethora of Pd, Co, and sum peaks, at high signal-to-noise ratio. Aside from some instrumentation artifacts (labeled with asterisks in Fig. 2(e)),

almost all aspects of these spectra are reproduced by a GUPIXWIN (65) simulation for PdCoO<sub>2</sub>, shown as the black line. The inset to Fig. 2(e), however, shows a close-up of the 4.5 to 7.3 keV region (shaded gray in the main panel), highlighting two peaks that are *not* accounted for by Pd, Co, or O. These peaks also exhibit crystal-to-crystal variations in intensity, strongly suggesting that they derive from trace impurities. The ~5.4 keV peak very likely indicates Cr impurities, while the 6.4 keV peak is very likely due to Fe (K<sub>α</sub>). Full quantification of impurity concentrations at this level is challenging for PIXE but our best estimates based on GUPIXWIN fits to Pd *L*, Co *K*, and Fe *K* peaks suggest Fe concentrations of  $\gtrsim 50$  ppm. (As for all impurity concentrations in this paper, this value is on a weight basis, *i.e.*, it is in  $\mu\text{g/g}$ ). While this is only approximate, this is a first indication that even CVT-grown PdCoO<sub>2</sub> crystals may not actually be ultrapure. As a final comment on these PIXE data, we note that Cl was not detected; the estimated limit of detection is of order 1000 ppm, however, due to overlap of Cl *K* and Pd *L* peaks.

### **Electronic and magnetic properties**

Electronic transport is an excellent relative probe of total defect and impurity densities, and thus *T*-dependent  $\rho_{\text{ab}}$  measurements were made on the new CVT-grown crystals. It is essential to acknowledge at this point that such measurements are nontrivial for single-crystal PdCoO<sub>2</sub> (17, 25, 49, 52), because of the extremely small low-*T* resistances (due to the very low residual  $\rho_{\text{ab}}$ ), and the sizable *c*-axis/*a*-*b* plane resistance anisotropy (~350-750, depending on *T* (8, 14–16)). The most accurate measurements in the literature in fact use focused ion beam techniques to pattern structures with long channel lengths to increase resistance, at the same time fully constraining the current path in the *a*-*b* plane (17, 25, 49, 52). In our case, the availability of larger crystals than in prior work enabled cleavage into relatively long and thin bar-shaped samples for simpler, in-line,

top-contact, four-wire measurements. The inset to Fig. 3(a) shows an example of such an in-line geometry on a 1.2-mm-long, 23- $\mu\text{m}$ -thick crystal. Even in this case, residual resistances were found to be  $\sim 20 \mu\Omega$ , necessitating low-noise measurements and careful accounting for instrumental offset voltages. Full details on this are provided in Methods and Supplementary Materials Section C. Briefly, an AC resistance bridge with a pre-amplifying channel scanner was employed, using parallel measurements on superconducting V thin films to determine and account for offsets. Top-contact geometries such as those shown in the inset to Fig. 3(a) are also subject to systematic error due to the large  $\rho_c/\rho_{ab}$  (8, 14–16). As described in Supplementary Materials Section C, finite-element simulations of current flow and potential drop were thus performed in our specific measurement geometry. These confirm overestimation of  $\rho_{ab}$  due to the large  $\rho_c$  that generates potential drop through the crystal thickness. This issue worsens with cooling (as  $\rho_c/\rho_{ab}$  increases), meaning, importantly, that RRR values in this geometry represent lower bounds on true values (see Supplementary Materials Section C for details).

Based on the above procedures, presented in Fig. 3(a) is  $\rho_{ab}(T)$  for the representative CVT-grown  $\text{PdCoO}_2$  crystal shown in the inset; Fig. 3(b) shows the same data on a  $\log_{10}$ - $\log_{10}$  scale. The 300 K resistivity of this representative crystal is  $3.65 \mu\Omega\text{cm}$ , which can be compared to reported values of 2.0–6.9  $\mu\Omega\text{cm}$  using standard contact methods (8, 14–16) and 3.1  $\mu\Omega\text{cm}$  using more accurate focused-ion-beam-patterned geometries (17). Our value of  $3.65 \mu\Omega\text{cm}$  is thus indeed slightly larger than the most accurate determination of 3.1  $\mu\Omega\text{cm}$  (17), but within the bounds expected for overestimation of  $\rho_{ab}$  due to the top-contact geometry (see Supplementary Materials Section C). On cooling, the  $\rho_{ab}(T)$  of this crystal saturates below 10–20 K, reaching a measured value of 8 n $\Omega$  cm. Taking this at face value, and considering the residual resistivity measurement uncertainty

(dominated by offset subtraction), a RRR of  $436 \pm 25$  is indicated. As noted above and discussed in detail in Supplementary Materials Section C, however, this RRR represents a lower bound due to the top-contact geometry. Finite element simulations suggest a true residual  $\rho_{ab}$  of  $\sim 4.4$  n $\Omega$  cm, yielding an actual RRR up to  $\sim 670$  (see Supplementary Materials Section C). Even without this correction, however, our measured RRR of  $\sim 440$  is a record in PdCoO<sub>2</sub>, which can be compared to 376 in prior metathesis/flux-grown crystals measured with focused-ion-beam patterning methods (17). In addition to realizing order-of-magnitude gains in crystal size and mass, our new CVT approach thus also results in measurably lower disorder in electronic transport.

Magnetometry measurements provide another probe of crystal quality and impurity concentrations in PdCoO<sub>2</sub> and were thus performed on CVT crystals. A typical result for the  $T$ -dependent molar susceptibility ( $\chi_{\text{mol}}$ ) is shown in Fig. 3(c). As illustrated by the black solid line, these data are well described by  $\chi_{\text{mol}}(T) = \chi_0 + C/(T - \theta)$ , *i.e.*, a sum of  $T$ -independent Pauli-related and  $T$ -dependent Curie-Weiss contributions, where  $C$  is the Curie constant and  $\theta$  is the Curie-Weiss temperature. The Pauli contribution derives from delocalized Pd  $d$  electrons, the  $\chi_{\text{Pauli}} = \frac{3}{2}\chi_0 = 1.65 \times 10^{-4}$  emu mol<sup>-1</sup> Oe<sup>-1</sup> (the factor of 3/2 accounts for Landau diamagnetism) in this case being near the middle of the distribution of literature values ( $0.9 \times 10^{-4}$  to  $2.9 \times 10^{-4}$  emu mol<sup>-1</sup> Oe<sup>-1</sup>, see Table 1). The low- $T$  Curie-Weiss tail, however, which should not ideally occur in PdCoO<sub>2</sub> (the Co<sup>3+</sup> ions are low-spin,  $S = 0$ ), very likely arises from local moments due to magnetic impurities. As shown in Table 1, the  $\theta = -2.6$  K extracted from the fit in Fig. 3(c) is indeed small, indicating weak inter-moment interactions, as would be expected of dilute impurities. This is reinforced by the inset to Fig. 3(c), where  $(\chi_{\text{mol}} - \chi_0)^{-1}$  is plotted *vs.*  $T$ , the 5 to 20 K fit yielding  $\theta = -2.0$  K.

Interestingly, the Curie constant extracted from the fit in Fig. 3(c) yields an effective number of Bohr magnetons ( $\mu_{\text{eff}}$ ) as high as  $0.09 \mu_{\text{B}}$  per formula unit (Table 1). Further insight into this is provided in Fig. 3(d), which shows the applied magnetic field ( $H$ ) dependence of the magnetization ( $M$ ) at 2 K, after correcting for  $\chi_0$ . The solid black line Brillouin fit captures the data moderately well, yielding a reasonable  $J = 1.2$ , along with a concentration of local moments corresponding to  $\sim 130$  ppm. (This is again on a weight basis; the atomic mass of Fe was assumed to convert from a number density of impurities (from the fit in Fig. 3(d)) to a weight-basis concentration). Taking this  $J$  and combining it with the Curie constants from the fits in Fig. 3(c) then yields local moment concentrations of  $\sim 200$  ppm. The low- $T$  paramagnetism in Figs. 3(c,d) can thus be consistently described by dilute, non-interacting local atomic moments, at concentrations of order 100 ppm. While some fraction of this Curie-tail magnetism no doubt arises from surface contamination, this is a second indication, along with PIXE data (Fig. 2(e)), that even CVT-grown  $\text{PdCoO}_2$  crystals host substantial impurity concentrations. Nevertheless, the  $\mu_{\text{eff}}$  values from the Curie-Weiss tails of CVT-grown crystals do represent a significant improvement over metathesis/flux crystals. This is emphasized in Table 1, which includes data from our metathesis/flux crystals, in addition to prior literature (14, 16, 53). The Curie-Weiss  $\mu_{\text{eff}}$  of our CVT crystals is over 4 times lower than our metathesis/flux crystals and is the lowest reported for  $\text{PdCoO}_2$ . Literature values on metathesis/flux-grown crystals in fact span 0.15 to  $0.78 \mu_{\text{B}}$  per formula unit (Table 1) (14, 16, 53), implying substantial magnetic impurity concentrations, even in crystals with large RRR (14). This apparent contradiction – clear indications of significant densities of magnetic impurities from magnetometry, in crystals that exhibit low disorder in transport – appears not to have been addressed in the literature. While CVT crystals are improved in this regard (they have the lowest  $\mu_{\text{eff}}$ ), and surface contributions are likely, the implied level of magnetic impurities is concerning.

For this reason, and to augment the chemical characterization in Figs. 2(d,e), we thus undertook trace impurity analysis *via* ICP-MS.

### **Impurity analysis**

As alluded to in the Introduction, ICP-MS-based trace impurity analysis on PdCoO<sub>2</sub> is complicated by the extraordinary acid etch resistance of metallic delafossites (43–45), which hinders simple acid digestion. We thus employed microwave digestion (see Methods for details), achieving complete digestion in ~15 bar of aqua regia or concentrated nitric acid vapor at 200 °C. ICP-MS was then performed on both metathesis/flux and CVT PdCoO<sub>2</sub>, quantifying the concentrations of 54 selected elements in a metals-basis approach (see Methods and Supplementary Materials Section D). This led to the immediate conclusion, contrary to the naïve view, that PdCoO<sub>2</sub> crystals are *not* generally ultrapure (Table 2). Averaged over multiple crystals and ICP-MS runs, the total metals-basis impurity concentration in our metathesis/flux crystals is in fact  $251 \pm 3$  ppm (Table 2, top panel). We emphasize that this value derives from the same synthesis method used in many prior reports on PdCoO<sub>2</sub> (5–8, 14–17, 22–27, 29–33, 49, 50, 53, 55) with  $\rho_{ab}$  down to 8 nΩ cm and RRR up to 376 (17). Our CVT crystals are purer, as might be expected of vapor-based growth, but still retain an average metals-basis impurity concentration of  $47 \pm 8$  ppm (Table 2, top panel).

Such substantial impurity concentrations, which are broadly consistent with PIXE and magnetometry (Figs. 2(e) and 3(c,d)), frame a central question for the remainder of this work: How can the record residual  $\rho_{ab}$  of these materials, and their exceptional RRR, be reconciled with such impurity concentrations? To underscore the importance of this question, note that the reported 20- $\mu$ m low- $T$  mean-free-path of PdCoO<sub>2</sub> would require impurity concentrations several orders-of-

magnitude lower than the above ICP-MS values, a point that we return to quantitatively below. Analysis of the *distribution* of the detected impurity elements casts much light on this issue. To this end, we first elaborate a simple classification scheme for the various substitutional elemental impurities that can be accommodated in PdCoO<sub>2</sub>. Fig. 4(a) depicts the crystal structure of PdCoO<sub>2</sub>, along with a classification for potential A- and B-site impurities in the ABO<sub>2</sub> delafossite structure. The critical point here is that, very unlike ABO<sub>3</sub> perovskites for example, there is a massive asymmetry in the number of elements that can conceivably populate A vs. B sites. This arises because the B-site in metallic ABO<sub>2</sub> delafossites involves a common cation valence in oxides (3+) and a common coordination with O<sup>2-</sup> (octahedral); this is as in perovskites, which can accommodate much of the periodic table on the B site. The A-site in metallic ABO<sub>2</sub> delafossites, on the other hand, involves a relatively uncommon valence in oxides (1+) and a far less common coordination with O<sup>2-</sup> ions (linear, see the structure in Fig. 4(a)). This situation, which contrasts starkly with ABO<sub>3</sub> perovskites, greatly reduces the possible accommodation of A-site vs. B-site substitutional impurities in ABO<sub>2</sub> compounds.

Considering this in more detail, as shown in Fig. 4(a), potential A-site-substituting impurities can be classified in terms of elements that are known to adopt the A-site in ABO<sub>2</sub> compounds, that either can (dark yellow) or cannot (light yellow) feasibly substitute for Pd in PdCoO<sub>2</sub>. We determine this feasibility by applying Goldschmidt-type criteria, requiring <30% ionic size mismatch, an ability to adopt the required coordination, and valence within  $\pm 1$  of the host element. Fig. 4(b) then shows a periodic table of select elements most relevant to ABO<sub>2</sub> compounds, labeled with their valence, coordination number, and ionic radii in the state most closely matching the delafossite structure. As shown in the figure, Li<sup>+</sup>, Na<sup>+</sup>, K<sup>+</sup>, Rb<sup>+</sup>, Cu<sup>+</sup>, Ag<sup>+</sup>, Pt<sup>+</sup>, and Hg<sup>2+</sup> (shaded yellow) are known to adopt the A-site in ABO<sub>2</sub> compounds, but in most cases cannot feasibly

substitute for Pd in PdCoO<sub>2</sub>. In particular, Li<sup>+</sup>, Na<sup>+</sup>, K<sup>+</sup>, and Rb<sup>+</sup> (light yellow) only form ABO<sub>2</sub> compounds with distinctly different structure to delafossite PdCoO<sub>2</sub>, with large coordination number with O<sup>2-</sup>. In most cases their ionic radii in this coordination are also far beyond the 30% mismatch for feasible substitution for Pd. In fact, the elements that can feasibly substitute for Pd in PdCoO<sub>2</sub> (dark yellow) number only four: Cu, Ag, Pt, and Hg, highlighted *via* the bold border in Fig. 4(b). Hg substitution would also be a special case, as the 2+ valence (Hg does not typically adopt 1+ valence in 2-fold coordination) would require an additional charge-balancing defect. This is supported by prior work on deliberately Mg-substituted PdCoO<sub>2</sub>, where A-site substitution with Mg<sup>2+</sup> was argued against based on similar arguments (66). The situation on the B site is very different. As shown in Fig. 4(a), potential B site substituents can be classified in terms of those that are known to adopt the B site in delafossites and can feasibly substitute for Co (darkest blue), those that are known to adopt the B site in ABO<sub>2</sub> compounds but cannot feasibly substitute for Co (lightest blue), and those for which it is unknown whether they form ABO<sub>2</sub> compounds but do fit the Co site in PdCoO<sub>2</sub> (intermediate blue). Again, feasibility is based on <30% size mismatch, 3±1 valence, and octahedral coordination. As shown in Fig. 4(b), the total group of possible B-site substituents is numerous, totaling at least 40 (all blue shades), remaining as high as 20 even after applying our fit criteria (darkest blue shades). In contrast to ABO<sub>3</sub> perovskites, the fundamental crystal chemistry of the ABO<sub>2</sub> delafossites thus results in a large asymmetry between the number of elements that can exist as substitutional impurities on the A and B sites.

Fig. 4(c) next maps the measured average concentrations of various ICP-MS-detected elements in CVT-grown PdCoO<sub>2</sub> crystals on to the classification scheme in Figs. 4(a,b). This periodic table employs the log<sub>10</sub> color scale of average impurity concentrations shown to the right, also labeling the concentration and limit of detection beneath each element. The conclusion is simple.

Substantial concentrations are found of elements that are likely to populate the Co site in PdCoO<sub>2</sub> (e.g., Mn, Fe, Ni, Al, Cr, Ir, Sn; the darker blue shades in Fig. 4(b)), but not of elements that can feasibly populate the Pd site. Neither Cu, Ag, Pt, or Hg (in the dark border in Figs. 4(b,c)) reach even 1 ppm in CVT crystals. These findings are further quantified in Table 2, where the top panel summarizes the total impurity concentrations of the elements likely to populate the Pd and Co sites in PdCoO<sub>2</sub>. In metathesis/flux crystals, of the total impurity concentration of 251 ppm (far right, Table 2), at least 132 ppm are elements that would be expected to populate the Co site (darkest blue shades in Fig. 4(b)), whereas only 4.4 ppm are elements that could feasibly populate the Pd site (Cu, Ag, Pt, Hg, dark yellow in Fig. 4(b)). We thus define a “sublattice purification ratio” of  $4.4/251 = 1.8\%$  of the total impurity concentration that could feasibly substitute for Pd. As also shown in the top panel of Table 2, the equivalent for CVT PdCoO<sub>2</sub> is  $1.9/47 = 4.0\%$  of the total average impurity concentration that could feasibly substitute for Pd, in this case only 1.9 ppm.

The middle and bottom panels of Table 2 break these concentrations down further, into the only four elements that can feasibly populate the Pd site (middle panel) and the most prevalent elements likely to populate the Co site (bottom panel). The former group consists of only Ag, Hg, Cu, and Pt, while the latter group includes Al, Cr, Mn, Fe, and Ni. Notable here is that one of the largest differences between CVT and metathesis/flux crystals is the decrease in Al, possibly due to the high thermal stability and low volatility of Al oxides. Another difference is the non-negligible concentration of impurities in metathesis/flux crystals that are not obviously capable of populating either the A or B sites. Surface contamination, strained B-site accommodation, and uptake in the minor impurity phases sometimes detected in metathesis/flux crystals (see Fig. S3(a) and associated discussion) can likely account for this. The concentrations of Cr, Mn, Fe, and Ni are also of particular interest, due to their likely magnetic character, no doubt contributing to the Curie-

Weiss susceptibility in Figs. 3(c,d) and Table 1. Quantitatively, the estimated magnetic impurity concentration from the bottom panel of Table 2 is 31 ppm in CVT crystals, compared to order 100 ppm from magnetometry. This is reasonable agreement considering the likelihood of additional surface contamination in magnetometry. In terms of comparisons to PIXE, ICP-MS on CVT crystals indicates  $9 \pm 2$  ppm of Fe, also comparing reasonably to the order-50-ppm approximate estimate from PIXE (Fig. 2(e)). Finally, ICP-MS was also used to determine the Pd/Co ratio of CVT crystals, yielding  $1.08 \pm 0.02$ . This is inconsistent with the EDS result of  $0.98 \pm 0.05$  at first sight, but EDS data were acquired from  $25 \times 25 \mu\text{m}^2$  regions free of surface particles. These particles are of course not excluded from ICP-MS, and thus remnant surface Pd and PdCl<sub>2</sub> likely skews the ICP-MS Pd/Co ratio.

## DISCUSSION

The conclusion from the above is that the prototypical metallic delafossite PdCoO<sub>2</sub> is by no means ultrapure in general terms. Total metals-basis impurity concentrations decrease from  $\sim 250$  ppm in metathesis/flux crystals to  $\sim 50$  ppm in CVT crystals, but remain substantial. Crystal-chemical principles, however, dictate that the great majority of substitutional impurities must reside on the Co site, the relatively rare valence and coordination on the Pd site resulting in few elemental impurities (particularly Cu, Ag, and Pt) being capable of substitution. Sublattice purification ratios of  $\sim 1\%$  thus arise, limiting the substitutional impurities on the Pd site to  $\sim 1$  ppm. Our simple conclusion from these findings is that the electronic conduction in metallic delafossites such as PdCoO<sub>2</sub>, which is strongly restricted to Pd *d* states at the Fermi level (5, 10, 18–21), thus occurs in highly pure Pd planes, with minimal substitutional impurities. This sublattice purification naturally explains how ultralow residual  $\rho_{ab}$  and extraordinary mean-free-paths can arise in

metallic delafossite single crystals, despite the relatively dirty methods employed in their synthesis (5, 49). Directly addressing a question posed in recent work (49), the BO<sub>6</sub> octahedral planes in metallic delafossites thus *do* host substantial disorder, in contrast to the Pd/Pt sheets, which were deduced to be highly perfect (49). The apparent contradiction of sizable magnetic impurity concentrations in crystals with high RRR is thus naturally resolved, as the majority of substitutional impurities, including magnetic ones, populate only the CoO<sub>6</sub> octahedra.

The above picture is predicated, however, on two key assumptions: that the ~1 ppm deduced impurity concentrations in the Pd planes are sufficiently low to facilitate the observed residual  $\rho_{ab}$  and mean-free-paths, and that the significant impurity concentrations in the BO<sub>6</sub> octahedral planes have sufficiently little impact on conduction in the Pd sheets. The first assumption can be addressed using the 2D unitary scattering approach recently applied by Sunko *et al.*, which was validated in irradiated metallic delafossite crystals (49). This essentially assumes the strongest possible *s*-wave scattering (49) in a Drude model, resulting in  $\rho = \frac{4\hbar n_d}{e^2 n}$ , where  $\hbar$  and  $e$  are the reduced Planck constant and electronic charge,  $n_d$  is the areal defect density, and  $n$  is the volume carrier density. Based on this, our deduced residual  $\rho_{ab}$  of 4 nΩcm would require a 2D defect density of  $6 \times 10^9$  cm<sup>-2</sup> in CVT-grown PdCoO<sub>2</sub>. Remarkably, this is in striking agreement with our determined Pd-sheet impurity density, which corresponds to  $5 \times 10^9$  cm<sup>-2</sup> based on the 1.9 ppm of A-site impurities in Table 2. (This calculation takes into account the exact A-site impurity elements in Table 2, and their relative masses). This indicates *quantitative* agreement between our deduced A-site impurity concentration and measured residual resistivity. This extends also to flux/metathesis crystals, where the A-site impurity concentration of 4.4 ppm in Table 2 would be expected to generate a residual  $\rho_{ab}$  of 7 nΩcm, remarkably close to measured values (17). (Again, this calculation takes

into account the exact A-site impurity elements in Table 2, and their relative masses; the distribution of impurities is different for CVT and metathesis/flux crystals). The second assumption is also supported by the recent work of Sunko *et al.*, which explicitly concluded that disorder in the B-O layers must be efficiently screened (49); the extent of this disorder was not determined in that paper, but is now known to be substantial (of order 100's of ppm).

Density functional theory (DFT) calculations provide further support for the above. These were performed (see Methods) on PdCoO<sub>2</sub> lightly-substituted with Pt, Fe, and Al, *i.e.*, a known impurity on the Pd site and two prevalent impurities on the B site.  $3 \times 3 \times 3$  supercells containing a single substituent atom were employed, *i.e.*, 3.7% concentrations, as a computationally-tractable approximation to the dilute limit. Unfolding of supercell bands was used to determine the effect of these impurities on the band structure and density-of-states (DOS) within the PdCoO<sub>2</sub> primitive cell. Fig. 5 shows the resulting band structures in the left panels (a-c) and the corresponding DOS in the right panels (d-f). As might be expected, dilute Pt impurities on the A site (Figs. 5(a,d)) have little effect on the band structure and DOS. The Pd *d*-band crossing the Fermi energy ( $E_F$ ) has no visible distortion at  $E_F$  in Fig. 5(a), and the atom-projected DOS in Fig. 5(d) is of very similar form for Pd and Pt. Note here that the simulated Pd<sub>0.963</sub>Pt<sub>0.037</sub>CoO<sub>2</sub> has 26-times more Pd than Pt but no normalization is applied in Figs. 5(d-f), simply to promote visibility of the impurity DOS.

As might also be anticipated, the situation for Fe impurities on the B site is more complex. A narrow impurity band forms below  $E_F$  (Fig. 5(b)), generating a clear peak in the Fe-projected DOS in Fig. 5(e). Nevertheless, this main impurity band peak is centered at  $\sim 0.2$  eV below  $E_F$  (many times  $k_B T$  at the temperatures of interest in this work), and is quite narrow, meaning that the impact at  $E_F$  remains negligible even for Fe impurities. This directly supports the above conclusion that

typical transition-metal B-site impurities (which are present at much lower concentrations in experiment) have only weak impact on conduction in the Pd planes of PdCoO<sub>2</sub>. For Al impurities (Figs. 5(c,f)), the absence of *d* electrons results in no significant effect on the band structure or DOS in the energy range in Figs. 5(c,f), the only impact being some smearing of existing bands. This smearing is likely related to the larger structural distortions induced by Al impurities relative to Fe and Pt. The Pd-Pd length for Pd ions bonded *via* O in AlO<sub>6</sub> octahedra shifts by as much as 0.6%, for example, 1.5 times more than the equivalent for Fe impurities, and 5 times more than for Pt. Similarly, the average bond length in AlO<sub>6</sub> octahedra differ by ~0.5% from the CoO<sub>6</sub> octahedra in pristine PdCoO<sub>2</sub>, much more than for the Fe case (0.02%). Figs. 5(b,c,e,f) thus establish that the B-site impurities Fe and Al indeed have greater impact on the electronic structure than the A-site impurity Pt (Figs. 5(a,d)), but with even Fe and Al having little meaningful impact in the vicinity of  $E_F$ , supporting our arguments.

It should be emphasized that the above analysis focuses on *substitutional* impurities. While *interstitial* impurities should also be considered, the delafossite structure is unlikely to host interstitial sites in which the ions in Fig. 4(b) can realistically be accommodated. The most obvious interstitial space involves an extra ion bonded to two O<sup>2-</sup> ions in the adjacent B-O layer, for which DFT calculations suggest a formation energy as high as 6.3 eV in the case of Pd interstitials (49), consistent with the low interstitial volume. The equilibrium concentrations of such defects would thus be negligible, and would decrease for larger Ag, Pt, and Hg interstitials. Beyond impurities, other point, line, and areal defects should be considered. As alluded to in the Introduction, however, current indications are that the densities of such defects are extraordinarily low in single-crystal metallic delafossites. This is supported by TEM observations (49, 55), deductions from irradiation-induced defect studies (49), the substantial formation energies for most point defects in

PdCoO<sub>2</sub> (49), and the various additional observations of structural quality in the current paper, most notably the X-ray rocking curve widths (Fig. 2(c) inset). Substitutional impurities thus appear to be the key defects in metallic delafossites, which have been comprehensively elucidated here. Future work to more completely understand the reasons for the low density of other point, line, and areal defects in these compounds is nevertheless clearly important.

In summary, this work establishes CVT as a highly promising approach to bulk single crystal growth of PdCoO<sub>2</sub>, with potential applicability to other metallic delafossites such as PdCrO<sub>2</sub> and PdRhO<sub>2</sub>. Compared to standard metathesis/flux methods, CVT generates orders-of-magnitude gains in crystal size and mass, along with the highest structural quality, highest purity, lowest magnetic impurity concentration, and highest RRR yet reported. Nevertheless, the first detailed trace impurity analysis of PdCoO<sub>2</sub> single crystals by ICP-MS reveals that, contrary to the naïve view, these metallic delafossites are *not* generally ultrapure; standard metathesis/flux methods result in ~250 ppm impurity concentrations, falling to ~50 ppm in CVT crystals. Simple crystal-chemistry-based analyses show that the vast majority of these impurities are forced to reside in the Co-O octahedral planes, however, only a small fraction being capable of substituting for Pd (typically a total of ~1 ppm of Cu, Ag, and Pt). The “sublattice purification ratio” is thus ~1%, resulting in ultrahigh purity in the Pd planes in which electronic conduction takes place, largely unaffected by the impurities in the CoO<sub>6</sub> octahedra. This sublattice purification mechanism is therefore central to the ultrahigh low-*T* conductivity of metallic delafossites, resolving the apparent contradiction that they appear impure from magnetometry yet highly pure in electronic transport. These results significantly demystify the outstanding low-*T* conductivity and mean-free-path in metallic delafossites, setting the stage for further advances with this extraordinary materials class. As an example, the analyses in Refs. (25, 30) place PdCoO<sub>2</sub> in a situation where the momentum-

conserving scattering rate is larger, but not much larger, than the momentum-relaxing scattering rate, leaving the system in a crossover regime between ballistic and viscous electronic transport. The momentum-conserving scattering is unlikely to be electron-electron scattering at the temperatures of interest (30) but could be electron-impurity scattering. It would thus be interesting to understand whether the Co-O plane impurities elaborated here could be responsible for such. More broadly, the concepts developed in this work can also be expanded to other metallic and semiconducting delafossites, and potentially to other complex crystal families with very different valence/chemical environments for different cations.

## **METHODS**

### **Crystal growth**

PdCoO<sub>2</sub> crystals were grown by two methods: the established metathesis/flux process (6) and our new CVT process (18). The established process utilizes the metathesis reaction  $\text{PdCl}_2 + \text{Pd} + \text{Co}_3\text{O}_4 \rightarrow 2\text{PdCoO}_2 + \text{CoCl}_2$  (6). Powders of PdCl<sub>2</sub> (Thermo Fisher Scientific, 99.999% purity), Pd (Sigma-Aldrich, 99.995%), and Co<sub>3</sub>O<sub>4</sub> (Alfa Aesar, 99.9985%) were mixed in a 1.5:1:1 molar ratio, then loaded and vacuum sealed (at 10<sup>-6</sup> Torr) in quartz ampoules; excess PdCl<sub>2</sub> is reported to promote crystallization of PdCoO<sub>2</sub> (14). Ampoules were then heated to 700-750 °C at a ramp rate of 300 °C/h in a box furnace, dwelled for 40-150 h, cooled to 400 °C at 40-60 °C/h, then furnace cooled to ambient. These conditions were fine-tuned to optimize yield and phase purity. To remove excess PdCl<sub>2</sub> and the reaction by-product CoCl<sub>2</sub>, the crystalline PdCoO<sub>2</sub> products (shown in Fig. 1(b)) were soaked in ethanol overnight then repeatedly washed in boiling ethanol until the effluent ran clear. Minor unreacted Pd and Co<sub>3</sub>O<sub>4</sub> phases were often detected in these

products by PXRD (see Supplementary Materials Section B). The largest crystals found in the products were  $0.8 \times 0.6 \text{ mm}^2$  laterally and 0.017 mm thick (Fig. 1(b), inset).

For CVT,  $\sim 1 \text{ g}$  of coarse-grained  $\text{PdCoO}_2$  product from the above metathesis reaction was mixed with  $\sim 120 \text{ mg}$  of  $\text{PdCl}_2$  powder, then loaded and vacuum sealed (at  $10^{-6}$  Torr) in quartz ampoules. Ampoules were then placed in a two-zone tube furnace with the reagents at one end of the ampoule (Fig. 1(a)). CVT was performed at a range of temperatures, spanning 740-800 °C for the hot zone and 680-750 °C for the cold zone. Hot- and cold-zone temperatures of 760 and 710 °C were found optimal in terms of crystal size and complete transport (*i.e.*, yield). For the first 3 days, the empty end of the tubes was maintained as the hot end, to clean the growth zone. The temperature gradient was then inverted for 13 days to establish the reagent-filled end of the tubes as the hot zone and the originally empty end as the cold/growth zone (Fig. 1(a)). We believe CVT to proceed *via* decomposition of  $\text{PdCl}_2$  (above  $\sim 600 \text{ °C}$  (57, 58)), followed by the reaction  $\text{PdCoO}_2(s) + 2\text{Cl}_2(g) \leftrightarrow \text{PdCl}_2(g) + \text{CoCl}_2(g) + \text{O}_2(g)$  (Fig. 1(a)). Multicrystals up to  $12 \times 12 \text{ mm}^2$  laterally and 0.3 mm thick result from this process (Fig. 1(c)). Single crystals were then isolated by gently breaking the multicrystals apart, generating up to  $6.0 \times 4.0 \text{ mm}^2$  lateral sizes, with thickness up to 0.17 mm (see Fig. 1(c), inset, for an example crystal). Excess chlorides were then removed by washing  $\text{PdCoO}_2$  crystals in boiling ethanol. We are aware of no prior report of such CVT growth of metallic delafossites, although one approach to  $\text{PdRhO}_2$  growth did employ a CVT-like temperature gradient (51) but with clear qualitative differences with our methods and findings.

### **Structural and chemical characterization**

Optical microscope images of crystals were acquired with a Zeiss Axiovert A1 MAT inverted microscope, while SEM was performed in a JEOL JSM-6010PLUS/LA. EDS data were taken with

an EDS detector integrated in the SEM, at 20 kV accelerating voltage. PIXE spectra were acquired in a MAS 1700 pelletron tandem ion accelerator (National Electrostatic Corp.) at 50  $\mu\text{C}$  dose from a 4 MeV  $\text{He}^{2+}$  beam; PIXE data were analyzed using GUPIXWIN (65). Laue diffraction, PXRd, and single-crystal HRXRD (including rocking curves) were taken using Photonic Science back-reflection Laue, Rigaku MiniFlex 600, and Rigaku SmartLab XE diffractometer systems, respectively, the latter two with  $\text{CuK}\alpha$  radiation. PXRd analysis employed JADE for whole pattern fits, which were used to determine  $a$  and  $c$  lattice parameters. Laue analysis employed Lauesim (67), modified for hexagonal symmetry.

### **Electronic transport and magnetometry measurements**

Single crystals for electronic transport were first cleaved into bar shapes (Fig. 3(a), inset) and affixed with GE varnish to  $\text{Al}_2\text{O}_3$  wafers. Al contact wires were attached in a four-point in-line geometry to the top surface of the  $\text{PdCoO}_2$  using ultrasonic wire bonding.  $T$ -dependent ( $\sim 4\text{-}300$  K) resistance measurements were then performed in a Janis cryostat/superconducting magnet, using a Lakeshore 370 AC resistance bridge and Lakeshore 3708 preamplifier/channel scanner (at 13.7 Hz and 10 mA). As alluded to in the main text and described in detail in Supplementary Material Section C, great care was taken to accurately determine and account for instrumental voltage offsets, which are important due to the very low low- $T$  resistance of  $\text{PdCoO}_2$ . A specialized protocol for this was developed and tested on zero-resistance superconducting V films. As also described in Supplementary Material Section C, finite element COMSOL simulations were performed to support the interpretation of the transport results, particularly with respect to the issue of systematic errors associated with the  $\rho_c/\rho_{ab}$  anisotropy. To minimize contamination for magnetometry measurements, crystals were first ground with thoroughly cleaned nonmagnetic tools then washed in ethanol to remove  $\text{CoCl}_2$ . The latter could occur not only at the original crystal

surfaces but also at internal inclusions/voids (16). Magnetometry was then done in a Quantum Design Physical Property Measurement System equipped with vibrating sample magnetometry (VSM) and high- $T$  options, from 2 to 600 K in magnetic fields to 7 T.

### **Impurity analysis**

For trace impurity analyses, ethanol-washed crystals were microwave digested in aqua regia (a 1:3 mixture of 70%-concentrated trace-metal-grade nitric acid (Ricca) and 36%-concentrated trace-metal-grade hydrochloric acid (Fisher Scientific)), or concentrated nitric acid, in sealed teflon pressure vessels. A CEM MARS 5 microwave digestion system was employed, reaching 200 °C and ~15 bar for 2 h. Solutions were allowed to slow cool to room temperature overnight before serial dilution and analysis; no visible solid remained. Trace element analysis in a Thermo Scientific iCap TQ triple quadrupole ICP-MS system was performed by standard addition methods using SPEX CertiPrep and ThermoFisher Scientific multielement standards. Internal standard sets included: Sc, Y, Ir for alkali metals, alkaline-earth metals, non-precious transition metals, metalloids, and heavy metals; Sc, Y, Bi for precious metals; V, Rb, Cs, Bi for Sc, Y, and rare-earth elements. ICP-MS analytical details for each element are listed in Table S6.

### **DFT calculations**

First-principles density functional theory calculations were performed with the Quantum ESPRESSO package using norm-conserving pseudopotentials, with the exchange-correlation energy approximated by the Perdew-Burke-Ernzerhof functional (68–70). The energy cutoff for the plane waves was set to 100 Ry. Dilute impurities on the Pd- and Co-sites (*i.e.*, Pd<sub>1-x</sub>Z<sub>x</sub>CoO<sub>2</sub> and PdCo<sub>1-x</sub>Z<sub>x</sub>O<sub>2</sub>) were simulated in a 3 × 3 × 3 supercell with 108 atoms, with one Pd or Co atom replaced, corresponding to  $x = 0.037$ . Pt substituted for Pd, and Fe and Al substituted for Co were considered. Both the unit cell shape and atomic positions were relaxed for electronic structure

calculations. The band structure and DOS were calculated on a  $\Gamma$ -centered Monkhorst-Pack grid of  $4 \times 4 \times 4$   $k$  points in the Brillouin zone of the supercell. The unfolded band structures in Fig. 5 were obtained using the bandUPpy code (71–73). The unfolding method projects a wave vector  $\underline{K}$  in the supercell Brillouin zone onto a corresponding wave vector  $\underline{k}$  in the primitive cell Brillouin zone *via* a supercell reciprocal lattice vector. This unfolding evaluates the spectral weight or probability of finding a set of primitive-cell Bloch states at wave vector  $\underline{k}$  that are contributing to the supercell eigenstates at wave vector  $\underline{K}$  at the same energy. The specific method adopted here (72) finds the effective band structure for doped PdCoO<sub>2</sub> by using the spectral function to calculate the weight, which is given by the number of primitive cell bands that are crossing within a small energy window around the band center.

## SUPPLEMENTARY MATERIALS

This PDF file includes: Sections A-D, Figs S1-S6, Tables S1-S7.

## REFERENCES AND NOTES

1. M. Imada, A. Fujimori, Y. Tokura, Metal-insulator transitions. *Rev. Mod. Phys.* **70**, 1039–1263 (1998).
2. H. Y. Hwang, Y. Iwasa, M. Kawasaki, B. Keimer, N. Nagaosa, Y. Tokura, Emergent phenomena at oxide interfaces. *Nat. Mater.* **11**, 103–113 (2012).
3. R. Ramesh, D. G. Schlom, Whither oxide electronics? *MRS Bull.* **33**, 1006–1014 (2008).
4. J. Mannhart, D. G. Schlom, Oxide interfaces - An opportunity for electronics. *Science.* **327**, 1607–1611 (2010).
5. A. P. Mackenzie, The properties of ultrapure delafossite metals. *Reports Prog. Phys.* **80**, 032501 (2017).
6. R. D. Shannon, D. B. Rogers, C. T. Prewitt, Chemistry of noble metal oxides. I. Syntheses and properties of ABO<sub>2</sub> delafossite compounds. *Inorg. Chem.* **10**, 713–718 (1971).
7. C. T. Prewitt, R. D. Shannon, D. B. Rogers, Chemistry of noble metal oxides. II. Crystal structures of platinum cobalt dioxide, palladium cobalt dioxide, copper iron dioxide, and silver iron dioxide. *Inorg. Chem.* **10**, 719–723 (1971).

8. D. B. Rogers, R. D. Shannon, C. T. Prewitt, J. L. Gillson, Chemistry of noble metal oxides. III. Electrical transport properties and crystal chemistry of  $ABO_2$  compounds with the delafossite structure. *Inorg. Chem.* **10**, 723–727 (1971).
9. R. Daou, R. Frésard, V. Eyert, S. Hébert, A. Maignan, Unconventional aspects of electronic transport in delafossite oxides. *Sci. Technol. Adv. Mater.* **18**, 919–938 (2017).
10. F. Lechermann, From basic properties to the Mott design of correlated delafossites. *npj Comput. Mater.* **7**, 120 (2021).
11. M. Mekata, N. Yaguchi, T. Takagi, S. Mitsuda, H. Yoshizawa, Magnetic ordering in delafossite  $CuFeO_2$ . *J. Magn. Magn. Mater.* **104–107**, 823–824 (1992).
12. F. Ye, J. A. Fernandez-Baca, R. S. Fishman, Y. Ren, H. J. Kang, Y. Qiu, T. Kimura, Magnetic interactions in the geometrically frustrated triangular lattice antiferromagnet  $CuFeO_2$ . *Phys. Rev. Lett.* **99**, 157201 (2007).
13. H. Kawazoe, M. Yasukawa, H. Hyodo, M. Kurita, H. Yanagi, H. Hosono, P-type electrical conduction in transparent thin films of  $CuAlO_2$ . *Nature.* **389**, 939–942 (1997).
14. H. Takatsu, S. Yonezawa, S. Mouri, S. Nakatsuji, K. Tanaka, Y. Maeno, Roles of high-frequency optical phonons in the physical properties of the conductive delafossite  $PdCoO_2$ . *J. Phys. Soc. Japan.* **76**, 104701 (2007).
15. C. W. Hicks, A. S. Gibbs, A. P. Mackenzie, H. Takatsu, Y. Maeno, E. A. Yelland, Quantum oscillations and high carrier mobility in the delafossite  $PdCoO_2$ . *Phys. Rev. Lett.* **109**, 116401 (2012).
16. M. Tanaka, M. Hasegawa, H. Takei, Growth and anisotropic physical properties of  $PdCoO_2$  single crystals. *J. Phys. Soc. Japan.* **65**, 3973–3977 (1996).
17. N. Nandi, T. Scaffidi, P. Kushwaha, S. Khim, M. E. Barber, V. Sunko, F. Mazzola, P. D. C. King, H. Rosner, P. J. W. Moll, M. König, J. E. Moore, S. Hartnoll, A. P. Mackenzie, Unconventional magneto-transport in ultrapure  $PdCoO_2$  and  $PtCoO_2$ . *npj Quantum Mater.* **3**, 66 (2018).
18. Y. Zhang, A. Saha, F. Tutt, V. Chaturvedi, B. Voigt, W. Moore, J. Garcia-Barriocanal, T. Birol, C. Leighton, Thermal properties of the metallic delafossite  $PdCoO_2$ : A combined experimental and first-principles study. *Phys. Rev. Mater.* **6**, 115004 (2022).
19. K. P. Ong, J. Zhang, J. S. Tse, P. Wu, Origin of anisotropy and metallic behavior in delafossite  $PdCoO_2$ . *Phys. Rev. B.* **81**, 115120 (2010).
20. V. Eyert, R. Frésard, A. Maignan, On the metallic conductivity of the delafossites  $PdCoO_2$  and  $PtCoO_2$ . *Chem. Mater.* **20**, 2370–2373 (2008).
21. K. Kim, H. C. Choi, B. I. Min, Fermi surface and surface electronic structure of delafossite  $PdCoO_2$ . *Phys. Rev. B.* **80**, 35116 (2009).
22. H.-J. Noh, J. Jeong, J. Jeong, E.-J. Cho, S. B. Kim, K. Kim, B. I. Min, H.-D. Kim, Anisotropic electric conductivity of delafossite  $PdCoO_2$  studied by angle-resolved photoemission spectroscopy. *Phys. Rev. Lett.* **102**, 256404 (2009).
23. F. Mazzola, V. Sunko, S. Khim, H. Rosner, P. Kushwaha, O. J. Clark, L. Bawden, I. Marković, T. K. Kim, M. Hoesch, A. P. Mackenzie, P. D. C. King, Itinerant ferromagnetism of the Pd-terminated polar surface of  $PdCoO_2$ . *Proc. Natl. Acad. Sci.* **115**, 12956–12960 (2018).

24. V. Sunko, thesis, Max Planck Institute for Chemical Physics of Solids, Dresden (2019).
25. P. J. W. Moll, P. Kushwaha, N. Nandi, B. Schmidt, A. P. Mackenzie, Evidence for hydrodynamic electron flow in PdCoO<sub>2</sub>. *Science*. **351**, 1061–1064 (2016).
26. C. Putzke, M. D. Bachmann, P. McGuinness, E. Zhakina, V. Sunko, M. Konczykowski, T. Oka, R. Moessner, A. Stern, M. König, S. Khim, A. P. Mackenzie, P. J. W. Moll, h/e oscillations in interlayer transport of delafossites. *Science*. **368**, 1234–1238 (2020).
27. H. Takatsu, J. J. Ishikawa, S. Yonezawa, H. Yoshino, T. Shishidou, T. Oguchi, K. Murata, Y. Maeno, Extremely large magnetoresistance in the nonmagnetic metal PdCoO<sub>2</sub>. *Phys. Rev. Lett.* **111**, 56601 (2013).
28. T. Harada, K. Sugawara, K. Fujiwara, M. Kitamura, S. Ito, T. Nojima, K. Horiba, H. Kumigashira, T. Takahashi, T. Sato, A. Tsukazaki, Anomalous Hall effect at the spontaneously electron-doped polar surface of PdCoO<sub>2</sub> ultrathin films. *Phys. Rev. Res.* **2**, 13282 (2020).
29. F. Mazzola, C.-M. Yim, V. Sunko, S. Khim, P. Kushwaha, O. J. Clark, L. Bawden, I. Marković, D. Chakraborti, T. K. Kim, M. Hoesch, A. P. Mackenzie, P. Wahl, P. D. C. King, Tuneable electron–magnon coupling of ferromagnetic surface states in PdCoO<sub>2</sub>. *npj Quantum Mater.* **7**, 20 (2022).
30. G. Baker, T. W. Branch, J. S. Bobowski, J. Day, D. Valentinis, M. Oudah, P. McGuinness, S. Khim, P. Surówka, Y. Maeno, R. Moessner, J. Schmalian, A. P. Mackenzie, D. A. Bonn, Non-local electro-dynamics in ultra-pure PdCoO<sub>2</sub>. arXiv:2204.14239 [cond-mat.mes-hall] (2023).
31. M. D. Bachmann, A. L. Sharpe, G. Baker, A. W. Barnard, C. Putzke, T. Scaffidi, N. Nandi, P. H. McGuinness, E. Zhakina, M. Moravec, S. Khim, M. König, D. Goldhaber-Gordon, D. A. Bonn, A. P. Mackenzie, P. J. W. Moll, Directional ballistic transport in the two-dimensional metal PdCoO<sub>2</sub>. *Nat. Phys.* **18**, 819–824 (2022).
32. M. D. Bachmann, A. L. Sharpe, A. W. Barnard, C. Putzke, M. König, S. Khim, D. Goldhaber-Gordon, A. P. Mackenzie, P. J. W. Moll, Super-geometric electron focusing on the hexagonal Fermi surface of PdCoO<sub>2</sub>. *Nat. Commun.* **10**, 5081 (2019).
33. P. H. McGuinness, E. Zhakina, M. König, M. D. Bachmann, C. Putzke, P. J. W. Moll, S. Khim, A. P. Mackenzie, Low-symmetry nonlocal transport in microstructured squares of delafossite metals. *Proc. Natl. Acad. Sci.* **118**, e2113185118 (2021).
34. J.-P. Doumerc, A. Wichainchai, A. Ammar, M. Pouchard, P. Hagenmuller, On magnetic properties of some oxides with delafossite-type structure. *Mater. Res. Bull.* **21**, 745–752 (1986).
35. M. Mekata, T. Sugino, A. Oohara, Y. Oohara, H. Yoshizawa, Magnetic structure of antiferromagnetic PdCrO<sub>2</sub> possible degenerate helices on a rhombohedral lattice. *Phys. B Condens. Matter.* **213–214**, 221–223 (1995).
36. H. Takatsu, H. Yoshizawa, S. Yonezawa, Y. Maeno, Critical behavior of the metallic triangular-lattice Heisenberg antiferromagnet PdCrO<sub>2</sub>. *Phys. Rev. B.* **79**, 104424 (2009).
37. H. Takatsu, G. Nénert, H. Kadowaki, H. Yoshizawa, M. Enderle, S. Yonezawa, Y. Maeno, J. Kim, N. Tsuji, M. Takata, Y. Zhao, M. Green, C. Broholm, Magnetic structure of the conductive triangular-lattice antiferromagnet PdCrO<sub>2</sub>. *Phys. Rev. B.* **89**, 104408 (2014).

38. H. Takatsu, S. Yonezawa, S. Fujimoto, Y. Maeno, Unconventional anomalous hall effect in the metallic triangular-lattice magnet PdCrO<sub>2</sub>. *Phys. Rev. Lett.* **105**, 137201 (2010).
39. J. M. Ok, Y. J. Jo, K. Kim, T. Shishidou, E. S. Choi, H.-J. Noh, T. Oguchi, B. I. Min, J. S. Kim, Quantum oscillations of the metallic triangular-lattice antiferromagnet PdCrO<sub>2</sub>. *Phys. Rev. Lett.* **111**, 176405 (2013).
40. E. Zhakina, R. Daou, A. Maignan, P. H. McGuinness, M. König, H. Rosner, S.-J. Kim, S. Khim, R. Grasset, M. Konczykowski, E. Tulipman, J. F. Mendez-Valderrama, D. Chowdhury, E. Berg, A. P. Mackenzie, Investigation of planckian behavior in a high-conductivity oxide: PdCrO<sub>2</sub>. arXiv:2301.10631 [cond-mat.str-el] (2023).
41. J. F. Mendez-Valderrama, E. Tulipman, E. Zhakina, A. P. Mackenzie, E. Berg, D. Chowdhury, T-linear resistivity from magneto-elastic scattering: application to PdCrO<sub>2</sub>. arXiv:2301.10776 [cond-mat.str-el] (2023).
42. S. Kumar, C. Multunas, B. Defay, D. Gall, R. Sundararaman, Ultralow electron-surface scattering in nanoscale metals leveraging Fermi-surface anisotropy. *Phys. Rev. Mater.* **6**, 85002 (2022).
43. T. Harada, Thin-film growth and application prospects of metallic delafossites. *Mater. Today Adv.* **11**, 100146 (2021).
44. T. Harada, Y. Okada, Metallic delafossite thin films for unique device applications. *APL Mater.* **10**, 70902 (2022).
45. T. Harada, S. Ito, A. Tsukazaki, Electric dipole effect in PdCoO<sub>2</sub>/β-Ga<sub>2</sub>O<sub>3</sub> Schottky diodes for high-temperature operation. *Sci. Adv.* **5**, eaax5733 (2019).
46. G. Li, S. Khim, C. S. Chang, C. Fu, N. Nandi, F. Li, Q. Yang, G. R. Blake, S. Parkin, G. Auffermann, Y. Sun, D. A. Muller, A. P. Mackenzie, C. Felser, In situ modification of a delafossite-type PdCoO<sub>2</sub> bulk single crystal for reversible hydrogen sorption and fast hydrogen evolution. *ACS Energy Lett.* **4**, 2185–2191 (2019).
47. B. Klobes, M. Herlitschke, K. Z. Rushchanskii, H.-C. Wille, T. T. A. Lummen, P. H. M. van Loosdrecht, A. A. Nugroho, R. P. Hermann, Anisotropic lattice dynamics and intermediate-phase magnetism in delafossite CuFeO<sub>2</sub>. *Phys. Rev. B.* **92**, 14304 (2015).
48. D. Bansal, J. L. Niedziela, A. F. May, A. Said, G. Ehlers, D. L. Abernathy, A. Huq, M. Kirkham, H. Zhou, O. Delaire, Lattice dynamics and thermal transport in multiferroic CuCrO<sub>2</sub>. *Phys. Rev. B.* **95**, 54306 (2017).
49. V. Sunko, P. H. McGuinness, C. S. Chang, E. Zhakina, S. Khim, C. E. Dreyer, M. Konczykowski, H. Borrmann, P. J. W. Moll, M. König, D. A. Muller, A. P. Mackenzie, Controlled introduction of defects to delafossite metals by electron irradiation. *Phys. Rev. X.* **10**, 21018 (2020).
50. R. Daou, R. Frésard, S. Hébert, A. Maignan, Large anisotropic thermal conductivity of the intrinsically two-dimensional metallic oxide PdCoO<sub>2</sub>. *Phys. Rev. B.* **91**, 41113 (2015).
51. P. Kushwaha, H. Borrmann, S. Khim, H. Rosner, P. J. W. Moll, D. A. Sokolov, V. Sunko, Y. Grin, A. P. Mackenzie, Single crystal growth, structure, and electronic properties of metallic delafossite PdRhO<sub>2</sub>. *Cryst. Growth Des.* **17**, 4144–4150 (2017).
52. P. Kushwaha, V. Sunko, P. J. W. Moll, L. Bawden, J. M. Riley, N. Nandi, H. Rosner, M. P. Schmidt, F. Arnold, E. Hassinger, T. K. Kim, M. Hoesch, A. P. Mackenzie, P. D. C. King, Nearly free electrons in a 5d delafossite oxide metal. *Sci. Adv.* **1**, e1500692 (2015).

53. M. Tanaka, M. Hasegawa, H. Takei, Crystal growth of PdCoO<sub>2</sub>, PtCoO<sub>2</sub> and their solid-solution with delafossite structure. *J. Cryst. Growth*. **173**, 440–445 (1997).
54. H. Takatsu, Y. Maeno, Single crystal growth of the metallic triangular-lattice antiferromagnet PdCrO<sub>2</sub>. *J. Cryst. Growth*. **312**, 3461–3465 (2010).
55. C. S. Chang, J. Sun, S. Khim, A. P. Mackenzie, D. G. Schlom, D. A. Muller, Visualization of defects in single-crystal and thin-film PdCoO<sub>2</sub> using aberration-corrected scanning transmission electron microscopy. *Phys. Rev. Mater.* **6**, 93401 (2022).
56. H. Usui, M. Ochi, S. Kitamura, T. Oka, D. Ogura, H. Rosner, M. W. Haverkort, V. Sunko, P. D. C. King, A. P. Mackenzie, K. Kuroki, Hidden kagome-lattice picture and origin of high conductivity in delafossite PtCoO<sub>2</sub>. *Phys. Rev. Mater.* **3**, 45002 (2019).
57. H. Renner, G. Schlamp, I. Kleinwächter, E. Drost, H. M. Lüscho, P. Tews, P. Panster, M. Diehl, J. Lang, T. Kreuzer, A. Knödler, K. A. Starz, K. Dermann, J. Rothaut, R. Drieselmann, C. Peter, R. Schiele, J. Coombes, M. Hosford, D. F. Lupton, "Platinum Group Metals and Compounds" in *Ullmann's Encyclopedia of Industrial Chemistry* (Wiley, New York, 2018), pp. 1–73.
58. M. A. Oranskaya, N. A. Mikhailova, Dissociation pressure and vapour pressure of palladium chloride. *Russ. J. Inorg. Chem.* **5**, 5–7 (1960).
59. B. Voigt, W. Moore, M. Manno, J. Walter, J. D. Jeremiason, E. S. Aydil, C. Leighton, Transport evidence for sulfur vacancies as the origin of unintentional n-Type doping in pyrite FeS<sub>2</sub>. *ACS Appl. Mater. Interfaces*. **11**, 15552–15563 (2019).
60. C. M. Brooks, L. F. Kourkoutis, T. Heeg, J. Schubert, D. A. Muller, D. G. Schlom, Growth of homoepitaxial SrTiO<sub>3</sub> thin films by molecular-beam epitaxy. *Appl. Phys. Lett.* **94**, 162905 (2009).
61. P. Ambwani, P. Xu, G. Haugstad, J. S. Jeong, R. Deng, K. A. Mkhoyan, B. Jalan, C. Leighton, Defects, stoichiometry, and electronic transport in SrTiO<sub>3-δ</sub> epilayers: A high pressure oxygen sputter deposition study. *J. Appl. Phys.* **120**, 55704 (2016).
62. E. Breckenfeld, R. Wilson, J. Karthik, A. R. Damodaran, D. G. Cahill, L. W. Martin, Effect of growth induced (non)stoichiometry on the structure, dielectric response, and thermal conductivity of SrTiO<sub>3</sub> thin films. *Chem. Mater.* **24**, 331–337 (2012).
63. T. Ohnishi, K. Shibuya, T. Yamamoto, M. Lippmaa, Defects and transport in complex oxide thin films. *J. Appl. Phys.* **103**, 103703 (2008).
64. B. Jalan, P. Moetakef, S. Stemmer, Molecular beam epitaxy of SrTiO<sub>3</sub> with a growth window. *Appl. Phys. Lett.* **95**, 32906 (2009).
65. GUPIXWIN, version 2.1.4, University of Guelph (2005); <https://www.physics.uoguelph.ca/about-gupix-and-gupixwin>.
66. M. Hasegawa, M. Tanaka, H. Takei, Metathetical reaction growth and characterization of delafossite-type Pd(Co,Mg)O<sub>2</sub> single crystals. *J. Cryst. Growth*. **226**, 277–280 (2001).
67. E. Pang, lauesim, GitHub (2019); <https://github.com/epang22/lauesim>.
68. P. Giannozzi, S. Baroni, N. Bonini, M. Calandra, R. Car, C. Cavazzoni, D. Ceresoli, G. L. Chiarotti, M. Cococcioni, I. Dabo, A. D. Corso, S. de Gironcoli, S. Fabris, G. Fratesi, R. Gebauer, U. Gerstmann, C. Gougoussis, A. Kokalj, M. Lazzeri, L. Martin-Samos, N. Marzari, F. Mauri, R. Mazzarello, S. Paolini, A. Pasquarello, L. Paulatto, C. Sbraccia, S. Scandolo, G. Sclauzero, A. P. Seitsonen, A. Smogunov, P. Umari, R. M. Wentzcovitch,

- QUANTUM ESPRESSO: a modular and open-source software project for quantum simulations of materials. *J. Phys. Condens. Matter.* **21**, 395502 (2009).
69. J. P. Perdew, K. Burke, M. Ernzerhof, Generalized gradient approximation made simple. *Phys. Rev. Lett.* **77**, 3865–3868 (1996).
  70. M. J. van Setten, M. Giantomassi, E. Bousquet, M. J. Verstraete, D. R. Hamann, X. Gonze, G.-M. Rignanese, The PseudoDojo: Training and grading a 85 element optimized norm-conserving pseudopotential table. *Comput. Phys. Commun.* **226**, 39–54 (2018).
  71. S. Tsirkin, A. Novianus, N. Cheng, bandUPpy, GitHub (2023); <https://github.com/band-unfolding/banduppy>.
  72. P. V. C. Medeiros, S. Stafström, J. Björk, Effects of extrinsic and intrinsic perturbations on the electronic structure of graphene: Retaining an effective primitive cell band structure by band unfolding. *Phys. Rev. B.* **89**, 41407 (2014).
  73. P. V. C. Medeiros, S. S. Tsirkin, S. Stafström, J. Björk, Unfolding spinor wave functions and expectation values of general operators: Introducing the unfolding-density operator. *Phys. Rev. B.* **91**, 41116 (2015).
  74. P. Villars, K. Cenzual, Eds., PdCoO<sub>2</sub> Crystal Structure: sd\_1920856. *PAULING FILE Inorg. Solid Phases* (2016); [https://materials.springer.com/isp/crystallographic/docs/sd\\_1920856](https://materials.springer.com/isp/crystallographic/docs/sd_1920856).
  75. R. D. Shannon, C. T. Prewitt, Effective ionic radii in oxides and fluorides. *Acta Crystallogr.* **B25**, 925–946 (1969).
  76. F. E. Wagner, S. Haslbeck, L. Stievano, S. Calogero, Q. A. Pankhurst, K.-P. Martinek, Before striking gold in gold-ruby glass. *Nature.* **407**, 691–692 (2000).
  77. M. Binnewies, R. Glaum, M. Schmidt, P. Schmidt, *Chemical Vapor Transport Reactions* (De Gruyter, Berlin, 2012).
  78. Chemical Rubber Company, *CRC Handbook of Chemistry and Physics* (CRC Press, Cleveland, Ohio, 2022).
  79. A. Wexler, W. S. Corak, Superconductivity of vanadium. *Phys. Rev.* **85**, 85–90 (1952).
  80. S. O. Kasap, *Principles of Electronic Materials and Devices* (McGraw-Hill Education, New York, ed. 4, 2018).

**Acknowledgments:** We thank Prof. Xinyuan Zhang for useful advice on ICP-MS analysis.

**Funding:** This work was primarily supported by the US Department of Energy through the University of Minnesota (UMN) Center for Quantum Materials, under Grant No. DE-SC0016371. Parts of this work were carried out in the Characterization Facility, UMN, which receives partial support from the National Science Foundation through the MRSEC (Award Number DMR-2011401) and NNCI (Award Number ECCS-2025124) programs. The Minnesota Supercomputing Institute at UMN provided resources that contributed to the research reported within this paper.

**Author contributions:** CL conceived the study and supervised its execution. YZ and FT grew the crystals, which were structurally and chemically characterized by YZ, FT, GH, MM, and JG-B. YZ, FT, BK, and JR performed the transport and magnetometry measurements. YZ, SB, and YT performed Laue characterization and analysis. YZ, GE, and WS performed mass spectrometry measurements and analysis. PS, TB, and RF performed the theoretical work. CL and YZ wrote the paper, with input from all authors.

**Competing interests:** The authors declare no competing interests.

**Data and materials availability:** All data needed to evaluate the conclusions presented in the paper are included in the paper and/or the Supplementary Materials. Digital data are available from the corresponding author upon reasonable request.

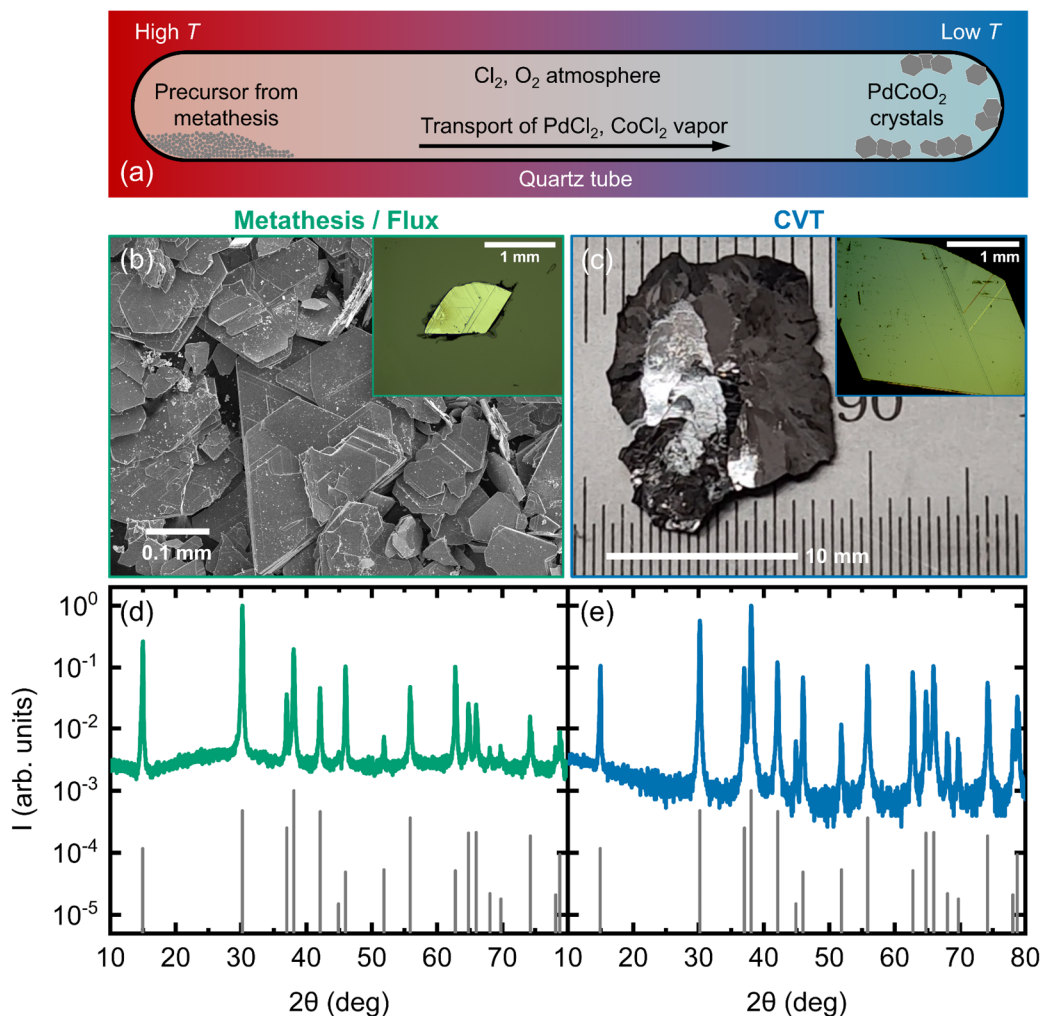


**Fig. 1. Crystal growth, microscopy, and powder X-ray diffraction for metathesis/flux and chemical vapor transport (CVT) crystals.** (a) Schematic of CVT growth of PdCoO<sub>2</sub>. (b,c) Images of the products of the metathesis/flux (b, scanning electron microscopy) and CVT (c, optical) methods. Insets: Optical microscopy images of typical single crystals from the metathesis/flux ( $0.8 \times 0.6 \times 0.017 \text{ mm}^3$ ) and CVT ( $3.5 \times 2.0 \times 0.17 \text{ mm}^3$ ) methods. (d,e) Powder X-ray diffraction patterns (intensity vs.  $2\theta$  angle) from representative ground crystals from the metathesis/flux ((d), green) and CVT ((e), blue) methods; reference patterns are shown in grey.

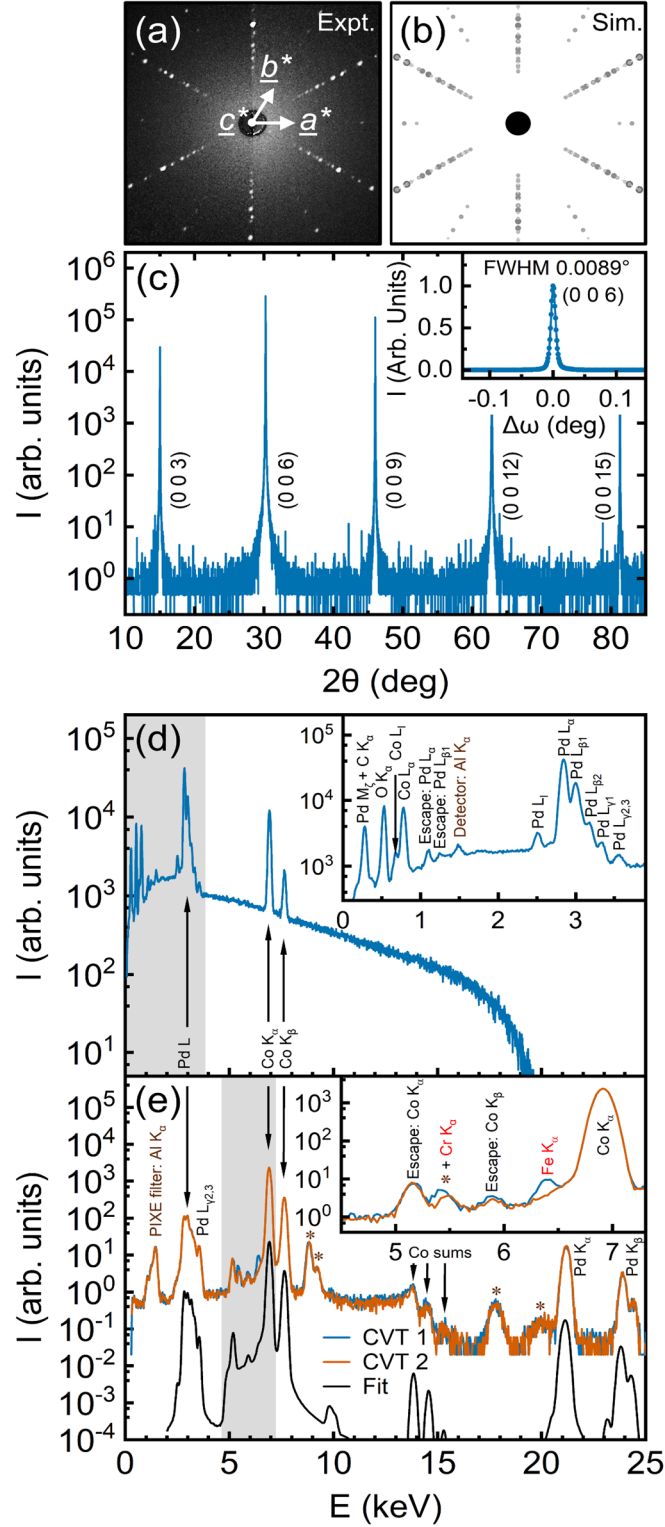


**Fig. 2. Structural and chemical characterization of CVT-grown single-crystal PdCoO<sub>2</sub>.** (a)

Back-reflection Laue X-ray diffraction pattern along a [001] zone axis of a representative single

crystal, with reciprocal-space axes labeled. (b) Corresponding simulated Laue pattern where the size of the points indicates their relative intensity and the central black circle represents the beam aperture. The simulation is based on the accepted PdCoO<sub>2</sub> structure and lattice parameters (6, 74). (c) Specular high-resolution X-ray diffraction (intensity vs. 2θ angle) from a representative 001-oriented single crystal, showing only 00l reflections. Inset: Rocking curve through the 006 reflection in (c), with a full-width-at-half-maximum (FWHM) of 0.0089°. (d) Energy-dispersive X-ray spectrum (intensity vs. energy) from a representative region (25 × 25 μm<sup>2</sup>) of a single crystal. The peaks are labeled and the inset is a close-up of the 0 to 3.9 keV region shaded grey. (e) Particle-induced X-ray emission spectra from two crystals (CVT 1 in blue and CVT 2 in orange), along with the GUPIXWIN simulation result discussed in the text (black, vertically offset for clarity). The peaks labeled with an “\*” are known instrumental artifacts in our ion beam accelerator/PIXE system. The inset is a close-up of the 4.5 to 7.3 keV region shaded grey; note the different intensities of the Cr and Fe K<sub>α</sub> peaks in the two crystals. The Cr peak at 5.4 keV has partial overlap with an artifact peak but the variation in intensity from crystal-to-crystal strongly suggests a contribution from Cr. The Fe peak at 6.4 keV has no such overlap and also varies from crystal-to-crystal.

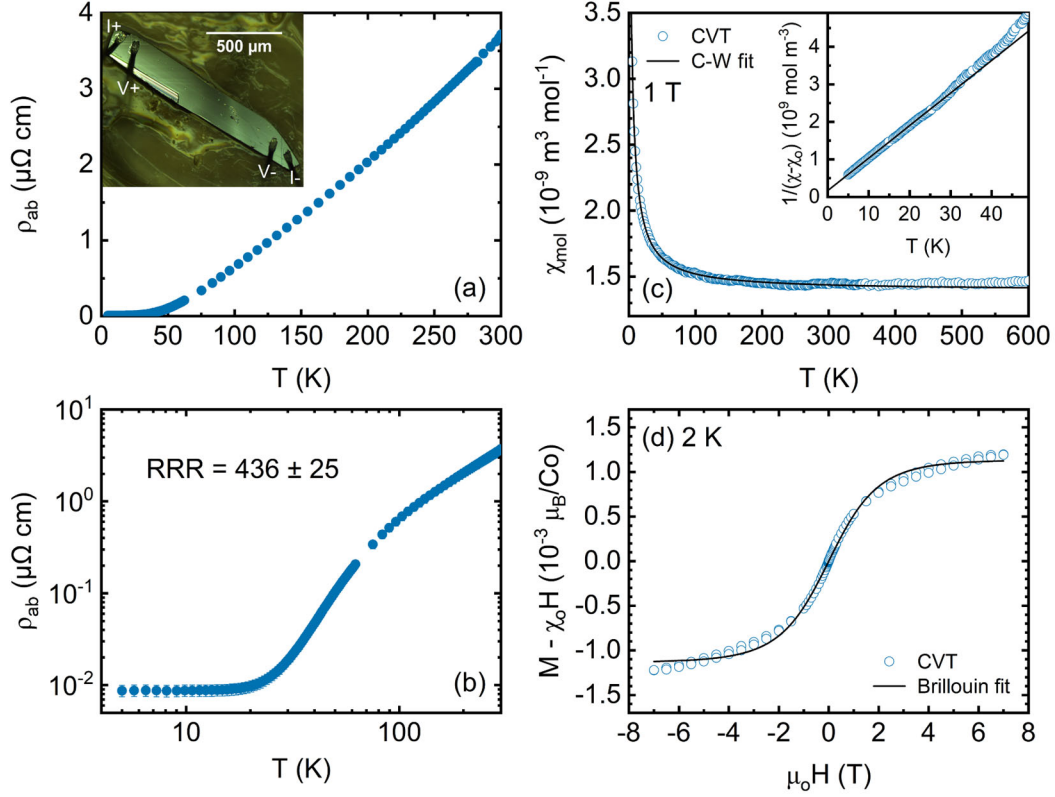
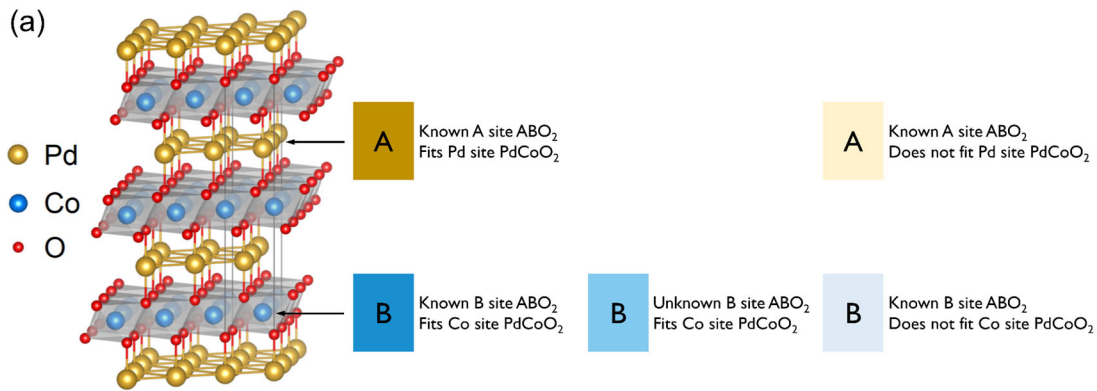


**Fig. 3. Electronic and magnetic properties of CVT-grown single-crystal PdCoO<sub>2</sub>.** (a)  $a$ - $b$ -plane resistivity ( $\rho_{ab}$ ) vs. temperature ( $T$ ) on a representative single crystal. Inset: Image of the crystal and four-point in-line contact arrangement. (b) Data from (a) on a log<sub>10</sub>-log<sub>10</sub> scale, highlighting the residual resistivity ratio of  $436 \pm 25$ . The error bars in (b) represent the uncertainty estimated from offset subtraction (dominant at low  $T$ ) and sample dimension measurements. (c) Molar magnetic susceptibility ( $\chi_{\text{mol}}$ ) vs.  $T$  in a 1 T magnetic field (blue open circles), from a representative powdered crystal. The black solid line is a fit to a sum of Pauli and Curie-Weiss susceptibilities, as discussed in the text. Inset:  $T$  dependence of  $(\chi_{\text{mol}} - \chi_0)^{-1}$ , where  $\chi_0$  is the  $T$ -independent susceptibility. The solid black line is a 5-20 K Curie-Weiss fit. (d) 2-K magnetization ( $M$ , corrected for  $\chi_0$ ) vs. magnetic field ( $\mu_0 H$ ) for the crystal in (c) (blue open circles). The solid black line is a Brillouin fit described in the text.



(b)

Valence — Coordination Number — Ionic Radius (pm)

|                    |                    |                     |                   |                   |                   |                        |                        |                   |                        |                    |                   |                   |                   |                    |                    |         |         |
|--------------------|--------------------|---------------------|-------------------|-------------------|-------------------|------------------------|------------------------|-------------------|------------------------|--------------------|-------------------|-------------------|-------------------|--------------------|--------------------|---------|---------|
| Li<br>1+, 6<br>74  | Be<br>2+, 6<br>35  |                     |                   |                   |                   |                        |                        |                   |                        |                    |                   | B<br>3+, 6<br>23  | C<br>-            | N<br>-             | O<br>-             | F<br>-  | Ne<br>- |
| Na<br>1+, 6<br>102 | Mg<br>2+, 6<br>72  |                     |                   |                   |                   |                        |                        |                   |                        |                    |                   | Al<br>3+, 6<br>53 | Si<br>4+, 6<br>40 | P<br>-             | S<br>-             | Cl<br>- | Ar<br>- |
| K<br>1+, 6<br>138  | Ca<br>2+, 6<br>100 | Sc<br>3+, 6<br>73   | Ti<br>3+, 6<br>67 | V<br>3+, 6<br>64  | Cr<br>3+, 6<br>61 | Mn<br>3+, 6<br>58 - 65 | Fe<br>3+, 6<br>55 - 65 | Co<br>3+, 6<br>53 | Ni<br>3+, 6<br>56 - 60 | Cu<br>1+, 2<br>46  | Zn<br>2+, 6<br>75 | Ga<br>3+, 6<br>62 | Ge<br>4+, 6<br>54 | As<br>3+, 6<br>58  | Se<br>-            | Br<br>- | Kr<br>- |
| Rb<br>1+, 6<br>149 | Sr<br>2+, 6<br>116 | Y<br>3+, 6<br>89    | Zr<br>4+, 6<br>72 | Nb<br>3+, 6<br>70 | Mo<br>3+, 6<br>67 | Tc<br>4+, 6<br>64      | Ru<br>3+, 6<br>68      | Rh<br>3+, 6<br>67 | Pd<br>1+, 2<br>59      | Ag<br>1+, 2<br>68  | Cd<br>2+, 6<br>95 | In<br>3+, 6<br>79 | Sn<br>4+, 6<br>69 | Sb<br>3+, 6<br>76  | Te<br>4+, 6<br>70  | I<br>-  | Xe<br>- |
| Cs<br>1+, 6<br>170 | Ba<br>2+, 6<br>136 | RE*<br>3+, 6<br>>85 | Hf<br>4+, 6<br>71 | Ta<br>3+, 6<br>67 | W<br>4+, 6<br>65  | Re<br>4+, 6<br>63      | Os<br>4+, 6<br>63      | Ir<br>4+, 6<br>63 | Pt<br>1+, 2<br>65      | Au<br>1+, 6<br>137 | Hg<br>2+, 2<br>69 | Tl<br>3+, 6<br>88 | Pb<br>4+, 6<br>78 | Bi<br>3+, 6<br>102 | Po<br>4+, 8<br>110 | At<br>- | Rn<br>- |

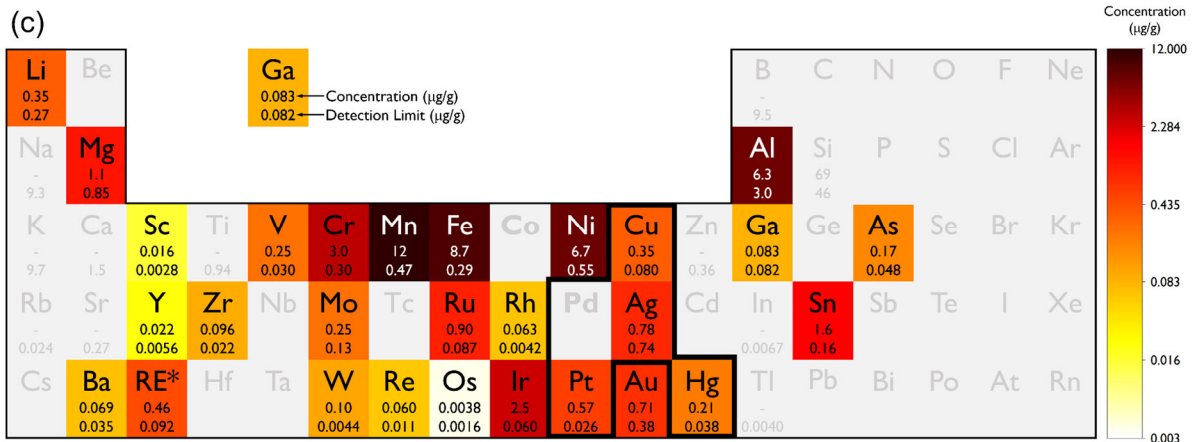


**Fig. 4. Impurity analysis of CVT-grown single-crystal  $PdCoO_2$ .** (a) Crystal structure of  $PdCoO_2$ . (b) Partial periodic table highlighting elements relevant to the delafossite structure. As defined in (a), light yellow highlights elements that are known to adopt the A site in  $ABO_2$

compounds but do not fit the Pd site in PdCoO<sub>2</sub>. Dark yellow highlights elements that are known to adopt the A site in delafossites and do fit the Pd site in PdCoO<sub>2</sub>; these are further highlighted by the bold black border. Analogously, the lightest blue color highlights elements that are known to adopt the B site in ABO<sub>2</sub> compounds but do not fit the Co site in PdCoO<sub>2</sub>, and the darkest blue highlights elements that are known to adopt the B site in delafossites and do fit the Co site in PdCoO<sub>2</sub>; the intermediate blue shade highlights elements for which it is unknown whether they adopt the B site in ABO<sub>2</sub> compounds but they do fit the Co site in PdCoO<sub>2</sub>. In this classification scheme, dark yellow highlights the elements likely to substitute for Pd (there are only four), while the two darker blue colors highlight the elements likely to substitute for Co (there are at least 20). Also shown for each element are the valence, coordination number, and ionic radius (75) in the state most closely relevant to the delafossite oxide structure. Where ranges of radii are provided this is for low- to high-spin states. Note that Au is not shaded dark yellow in (b); there exists some evidence of Au<sup>1+</sup> in linear coordination with O<sup>2-</sup> (76) but it is not common. (c) Partial periodic table labeled with the detected concentration and detection limit for each element probed in mass spectrometry. All values are in weight-basis ppm and are averaged over multiple runs and CVT crystals, as in Table 2. The color scale (right) is a log<sub>10</sub>-scale of the average impurity concentration in CVT crystals. As in (b), the bold black border highlights the elements likely to substitute for Pd; the total concentration of these elements is only 1.9 ppm. The entire rare-earth block of elements appears as “RE” in panels (b,c); in panel (c), the values are the sum totals for these RE elements. Na, B, and Si, which are common glassware impurities, were excluded from all ICP-MS analyses.

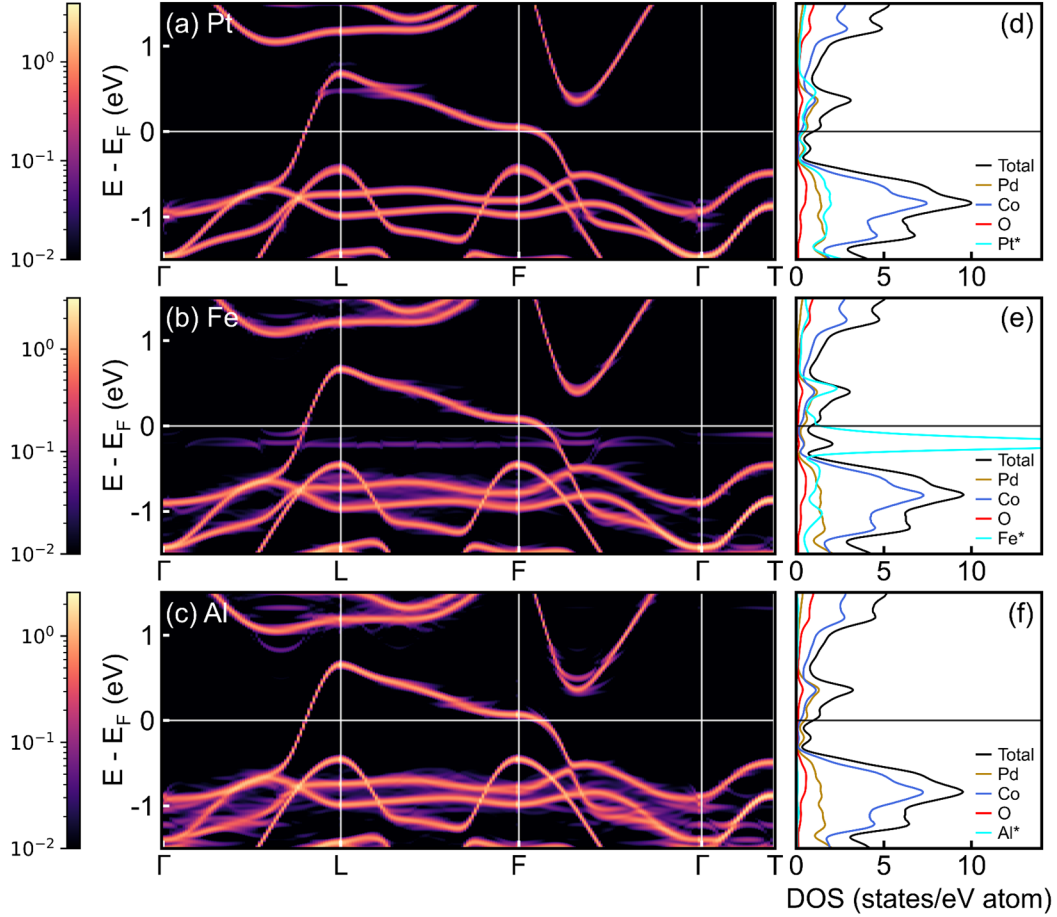


**Fig. 5. DFT-calculated electronic band structure and density-of-states of lightly-substituted PdCoO<sub>2</sub>.** (a)-(c) Band structure of Pd<sub>1-x</sub>Pt<sub>x</sub>CoO<sub>2</sub>, PdCo<sub>1-x</sub>Fe<sub>x</sub>O<sub>2</sub>, and PdCo<sub>1-x</sub>Al<sub>x</sub>O<sub>2</sub>, respectively, for  $x = 0.037$ , *i.e.*, 3.7% substitutional impurity density. Shown is the high-symmetry  $k$ -path  $\Gamma$ -L-F- $\Gamma$ -T, in the first Brillouin zone, with energies relative to the Fermi energy,  $E_F$ . The intensities are on a  $\log_{10}$  scale depicting the weight of the unfolded primitive cell bands obtained from the supercell bands *via* the unfolding method (72, 73). (d)-(f) Corresponding density-of-states (DOS). Shown are the total DOS (black), and the atom-projected DOS of Pd (dark yellow), Co (blue), O (red), and the respective impurity (cyan). The DOS values are for the primitive cell, calculated by dividing by the corresponding number of atoms in the supercell. The atom-projected DOS curves

for the impurity atoms (labeled with an asterisk) should thus be scaled by a factor of 0.037 for direct comparison; they are plotted here unscaled for improved visibility.

**Table 1.** Summary of parameters from analysis of magnetometry data on PdCoO<sub>2</sub> crystals in this work and in prior literature. Shown are the literature reference, measurement details, temperature-independent susceptibility ( $\chi_0$ ), Curie-Weiss temperature ( $\theta$ ), and effective number of Bohr magnetons from the low-temperature Curie-Weiss contribution ( $\mu_{eff}$ ). Note that the Pauli susceptibility can be calculated using  $\chi_{Pauli} = \frac{3}{2}\chi_0$ , as discussed in the text.

| Reference                         | Measurement details                     | $\chi_0$<br>(emu mol <sup>-1</sup> Oe <sup>-1</sup> ) | $\theta$<br>(K) | $\mu_{eff}$<br>( $\mu_B$ /formula unit) |
|-----------------------------------|---|---|-----------------|---|
| Tanaka <i>et al.</i> (1996) (16)  | Ground crystal                          | $1.9 \times 10^{-4}$                                  | -3.50           | 0.66                                    |
| Tanaka <i>et al.</i> (1996) (16)  | $\underline{H} \perp \underline{c}$     | $1.1 \times 10^{-4}$                                  | 10.63           | 0.69                                    |
| Tanaka <i>et al.</i> (1996) (16)  | $\underline{H} \parallel \underline{c}$ | $1.6 \times 10^{-4}$                                  | 0.69            | 0.57                                    |
| Tanaka <i>et al.</i> (1997) (53)  | Ground crystal                          | $0.6 \times 10^{-4}$                                  | -12.13          | 0.78                                    |
| Takatsu <i>et al.</i> (2007) (14) | $\underline{H} \perp \underline{c}$     | $1.9 \times 10^{-4}$                                  | -38.9           | 0.20                                    |
| Takatsu <i>et al.</i> (2007) (14) | $\underline{H} \parallel \underline{c}$ | $1.7 \times 10^{-4}$                                  | -40.8           | 0.15                                    |
| This work, metathesis/flux        | Ground crystal                          | $2.0 \times 10^{-4}$                                  | -8.1            | 0.37                                    |
| This work, CVT                    | Ground crystal                          | $1.1 \times 10^{-4}$                                  | -2.6            | 0.09                                    |

**Table 2.** Summary of average impurity concentrations (in weight-basis ppm) in metathesis/flux- and CVT-grown PdCoO<sub>2</sub> crystals, as determined by ICP-MS. The averages are over 2-3 runs on 1-3 crystals, and the uncertainties listed are standard deviations. Na, B, and Si, which are common glassware impurities, were excluded from all analyses. The detection limit (DL) is listed for each element; for concentrations below this detection limit, “BDL” is entered. Top panel. First column: total concentrations of elements known to adopt the A-site in ABO<sub>2</sub> compounds that also fit the Pd site in PdCoO<sub>2</sub>. Second column: total concentrations of elements known to adopt the A-site in ABO<sub>2</sub> compounds that do not fit the Pd site in PdCoO<sub>2</sub>. Third column: total concentrations of elements that fit the Co site in PdCoO<sub>2</sub>. Fourth column: total concentrations of elements known to adopt the B-site in ABO<sub>2</sub> compounds that do not fit the Co site in PdCoO<sub>2</sub>. Fifth column: concentration of all other elements measured (*i.e.*, those not in columns 1-4). Sixth column: Total of all prior columns. Middle panel. Concentrations of the only elements (four) that are known to adopt the A-site in ABO<sub>2</sub> delafossites and also fit the Pd site in PdCoO<sub>2</sub>. Bottom panel: Concentrations of the seven most prevalent elements that fit the Co site in PdCoO<sub>2</sub>.

### Total Impurities in PdCoO<sub>2</sub>

|             | Known A site ABO <sub>2</sub> , fits Pd site PdCoO <sub>2</sub> (µg/g) | Known A site ABO <sub>2</sub> , does not fit Pd site PdCoO <sub>2</sub> (µg/g) | Fits Co site, PdCoO <sub>2</sub> (µg/g) | Known B site ABO <sub>2</sub> , does not fit Co site PdCoO <sub>2</sub> (µg/g) | All other (µg/g) | Total (µg/g) |
|-------------|--|--|---|--|------------------|--------------|
| <b>Flux</b> | 4.41 ± 0.03  | 21 ± 2   | 132 ± 2                                 | 67 ± 1   | 27.3 ± 0.5       | 251 ± 3      |
| <b>CVT</b>  | 1.9 ± 0.3  | 0.4 ± 0.1  | 42 ± 7                                  | 0.6 ± 0.2  | 1.9 ± 0.6        | 47 ± 8       |

### A-site Elemental Impurities in PdCoO<sub>2</sub>

|             | Ag (µg/g)   | Hg (µg/g)   | Cu (µg/g)   | Pt (µg/g)   |
|-------------|-------------|-------------|-------------|-------------|
| <b>Flux</b> | 1.69 ± 0.01 | BDL         | 0.50 ± 0.03 | 2.22 ± 0.02 |
| <b>CVT</b>  | 0.78 ± 0.06 | 0.21 ± 0.02 | 0.4 ± 0.2   | 0.6 ± 0.2   |
| <b>DL</b>   | 0.74        | 0.038       | 0.080       | 0.026       |

### Most Prevalent B-site Elemental Impurities in PdCoO<sub>2</sub>

|             | Al (µg/g) | Cr (µg/g)   | Mn (µg/g)  | Fe (µg/g) | Ni (µg/g)  | Sn (µg/g)   | Ir (µg/g)   |
|-------------|-----------|-------------|------------|-----------|------------|-------------|-------------|
| <b>Flux</b> | 82 ± 2    | 3.22 ± 0.09 | 13.3 ± 0.2 | 9.2 ± 0.2 | 15.0 ± 0.2 | 2.49 ± 0.04 | 1.08 ± 0.01 |
| <b>CVT</b>  | 6.3 ± 0.8 | 3 ± 1       | 12 ± 6     | 9 ± 2     | 7 ± 3      | 1.61 ± 0.03 | 2.5 ± 1     |
| <b>DL</b>   | 3.0       | 0.30        | 0.47       | 0.29      | 0.55       | 0.16        | 0.06        |

**Supplementary Materials for:**  
**Crystal-Chemical Origins of the Ultrahigh Conductivity  
of Metallic Delafossites**

Yi Zhang (張易), Fred Tutt, Guy N. Evans, Prachi Sharma, Greg Haugstad, Ben Kaiser,  
Justin Ramberger, Samuel Bayliff, Yu Tao, Mike Manno, Javier Garcia-Barriocanal,  
Rafael M. Fernandes, Turan Birol, William E. Seyfried Jr., and Chris Leighton\*

\*Corresponding author. Email: leighton@umn.edu

**This PDF file includes:**

**Section A. Chemical Vapor Transport (CVT) Crystal Growth**

Figs. S1 and S2

**Section B. Specific Growth Parameters of Characterized Crystals**

Figs. S3

Tables S1 and S2

**Section C. Transport Measurement Details**

Figs. S4 to S6

Tables S3 to S5

**Section D. ICP-MS Trace Impurity Analysis Details**

Tables S6 and S7

References (77 to 80)

## Section A. Chemical Vapor Transport (CVT) Crystal Growth

**CVT Setup and Optimization.** As noted in the main text, while CVT has not been reported for PdCoO<sub>2</sub>, there are several reasons to consider this growth approach, including the fact that PdCoO<sub>2</sub> decomposes (6, 43, 45) and that PdCl<sub>2</sub> (which decomposes at ~600 °C in low Cl pressure (57, 58)) is a potentially convenient transport agent. CVT crystal growth of Co<sub>3</sub>O<sub>4</sub> (77), Pd (77), and PdO (77) have also been reported. A CVT process was thus designed based on the known properties of PdCoO<sub>2</sub>, PdCl<sub>2</sub>, and CoCl<sub>2</sub>.

CVT growth of Co<sub>3</sub>O<sub>4</sub>, Pd, and PdO using PdCl<sub>2</sub> as a transport agent have been reported at growth temperatures in the 400-1000 °C range (77), based on reactions such as  $Co_3O_4(s) + 3Cl_2(g) \rightleftharpoons 3CoCl_2(g) + 2O_2(g)$ ,  $Pd(s) + Cl_2(g) \rightleftharpoons PdCl_2(g)$ , and  $2PdO(s) + 2Cl_2(g) \rightleftharpoons 2PdCl_2(g) + O_2(g)$ . The decomposition of PdCoO<sub>2</sub> in air commences at ~800 °C (45), in the range of established CVT temperatures for Co<sub>3</sub>O<sub>4</sub>, Pd, and PdO (77). We therefore propose the analogous transport reaction,  $PdCoO_2(s) + 2Cl_2(g) \rightleftharpoons CoCl_2(g) + PdCl_2(g) + O_2(g)$ , where, in the forward reaction, solid PdCoO<sub>2</sub> is volatilized by Cl<sub>2</sub> vapor generated from partial thermal decomposition of PdCl<sub>2</sub>, then transformed into a mixture of gaseous CoCl<sub>2</sub>, PdCl<sub>2</sub>, and O<sub>2</sub> at the hot end of the growth ampoule. CoCl<sub>2</sub> and PdCl<sub>2</sub> vapors then transport across the temperature gradient, forming PdCoO<sub>2</sub> in the ampoule's cold end through the reverse reaction.

The choice of transport agent was also considered, *i.e.*, whether to use PdCl<sub>2</sub>, PdBr<sub>2</sub>, or PdI<sub>2</sub>, for example. For PdCoO<sub>2</sub> growth, the co-stability of halides of Co and Pd is essential. PdBr<sub>2</sub> and PdI<sub>2</sub> have very low decomposition points (250 and 360 °C, respectively (78)), much lower than the CoBr<sub>2</sub> and CoI<sub>2</sub> melting points (678 and 520 °C, respectively) (78). The bromides or iodides of Pd and Co having comparable vapor pressures at reasonable temperatures is thus unlikely. PdCl<sub>2</sub>, however, decomposes at 600-740 °C (the range is likely due to variable Cl<sub>2</sub> pressures) (57, 58), with a melting point at 680 °C (78), while CoCl<sub>2</sub> has a similar melting point of 737 °C (78); this suggests a reasonable likelihood of co-stability of their vapors at ~700 °C. PdCl<sub>2</sub> was therefore chosen as the transport agent, taking advantage of its partial thermal decomposition to generate Cl<sub>2</sub> at ~600 °C, without the use of hazardous Cl<sub>2</sub> gas, and avoiding potential impurities from Cl<sub>2</sub>-generating transport agents such as HgCl<sub>2</sub> (77).

As shown in Fig. S1(a), for CVT growth, vacuum-sealed quartz ampoules (see Methods) were held horizontally in a multi-zone furnace, with the precursor powders (~1 g of metathesis/flux-grown

PdCoO<sub>2</sub> and ~0.12g of PdCl<sub>2</sub>) loaded at the right end of the ampoule (in Zone 2), and the empty end of the ampoule in Zone 1. For the first 3 days, Zone 1 was the hot zone and Zone 2 the cold zone, while for the remaining 13 days the temperatures gradient was reversed; the rationale for this is provided below. A typical ampoule after the end of a CVT growth is shown in Fig. S1(b). At the end of a successful growth, essentially all of the PdCoO<sub>2</sub> is transported to the growth (cold) zone, forming PdCoO<sub>2</sub> single crystals, PdCoO<sub>2</sub> multicrystals, and excess chlorides. The other ampoule end is essentially empty, indicating high yield.

A 50 °C temperature difference was chosen for most growths in this work. Smaller differences, such as 30 °C, led to slow crystal growth rates and incomplete transport in 13 days, while larger differences, such as 60 °C, led to smaller crystal sizes, likely indicating too high a transport rate. Most growths were done with 710/760 °C cold/hot zone temperatures (such as the ampoule in Fig. S1(b)), which were found to yield the largest crystals, with reflective surfaces, and near-complete transport. Higher temperature conditions were experimented with, using 750/800 °C and 800/850 °C (the ampoules in Figs. S1(c,d), respectively), for example. At these higher temperatures, the yield of PdCoO<sub>2</sub> crystals decreased, with no improvement in crystal size. A magenta coating also developed on the inner ampoule walls, as in metathesis/flux growth at ≥750 °C, which was found by X-ray diffraction to be mainly Co<sub>2</sub>SiO<sub>4</sub>. This likely results from high-temperature side reactions between cobalt compounds and quartz. Eventually, in the 800/850°C growth, no PdCoO<sub>2</sub> crystals were grown, and PdO, along with <10 wt.% untransported PdCoO<sub>2</sub> precursor was found to remain in the hot zone. At these temperatures, PdCoO<sub>2</sub> likely decomposes into binaries at 850 °C, the resulting cobalt compounds reacting with the quartz to form the Co<sub>2</sub>SiO<sub>4</sub> tube coating in Fig. S1(d).

**CVT Mechanisms.** Based on the above, and on additional observations below, various conclusions can be reached regarding the mechanisms of CVT growth. The growth starts with the initial conditions in Fig. S2(a), with the mix of precursor powders located in Zone 2 and the nominally empty ampoule end in Zone 1. Note here that the “empty” end of the ampoule is inevitably unintentionally dusted with precursor powder particles during loading, as shown in Fig. S2(a). As it is common for metathesis/flux-grown PdCoO<sub>2</sub> (one of the precursors here) to have small amounts of impurity phases, including Pd (see Section B below), there are thus microscopic quantities of Pd present, as also shown in Fig. S2(a). In the first stage of the growth, illustrated in Fig. S2(b), the ampoule end filled with precursors is the cold zone (Zone 2) and the empty end is the hot zone

(Zone 1), for an inverted-temperature-gradient period of 3 days. The purpose of this first stage is to transport any PdCoO<sub>2</sub> powder particles in the “empty” end of the ampoule to the other end, hence “cleaning” the growth zone, *i.e.*, ridding it of stray nuclei. During this stage however, which was found to be essential, Pd (whether from phase impurities in the metathesis/flux-grown PdCoO<sub>2</sub> or partial thermal decomposition of PdCl<sub>2</sub>) will be transported to the empty ampoule end, as Pd is known to transport *via* Cl<sub>2</sub> from cool to hot (77); this is due to the exothermic  $Pd(s) + Cl_2(g) \rightarrow PdCl_2(g)$  reaction (77). The significance of this point is returned to below. The initial 3 days of inverted temperature gradient are followed by the main (13-day) growth stage shown in Fig. S2(c). At the start of this period, as explained above, the growth zone (Zone 1) can be expected to contain Pd crystallites (whether there originally, or transported from Zone 2). These Pd crystallites may then act as nucleation centers for PdCoO<sub>2</sub> crystal growth. Notably, the interatomic distance within the (111) planes of Pd is 0.275 nm (7), similar (within -2.8%) to the PdCoO<sub>2</sub> lattice parameter of  $a = 0.283$  nm (5–7). Pd particles can thus likely seed the PdCoO<sub>2</sub> CVT crystal growth in this process, which we propose as an explanation for the multicrystal formation that we found common. In essence, we propose that PdCoO<sub>2</sub> crystals can grow in multiple directions from different (111)-family facets of Pd crystallites, generating multicrystals. As noted in the main text, these multicrystals can be easily separated into single crystals, and some single crystals also form, presumably due to non-Pd-seeded growth. As a final comment on this mechanism, note that PdO may also play a similar role in nucleation.

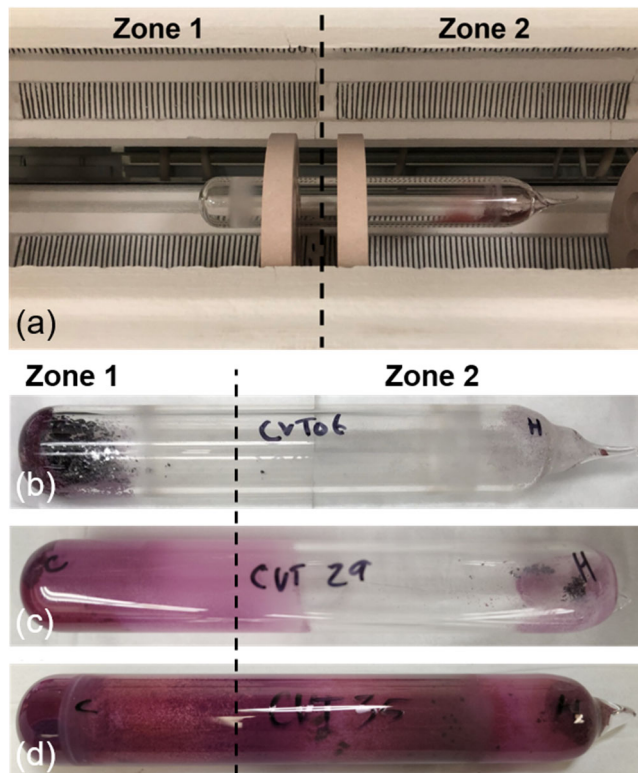


**Fig. S1. CVT growth setup and example ampoules.** (a) Two-zone furnace setup prior to CVT growth. The ~6-inch-long quartz ampoule is held between two zones labeled Zone 1 and Zone 2, with the boundary marked by the black dashed line. The precursor powders are loaded into the right side of the ampoule, in Zone 2. (b) Example quartz ampoule after a 710/760 °C CVT growth. “Zone 1”, “Zone 2”, and the dashed line mark the in-furnace position of the ampoule. CVT crystals are grown in the left side of the ampoule, in Zone 1, at essentially complete yield. (c) Example quartz ampoule after a 750/800 °C CVT growth. (d) Example quartz ampoule after a 800/850 °C growth. In (c,d), note the magenta coating inside the quartz tubes, identified as  $\text{Co}_2\text{SiO}_4$ .

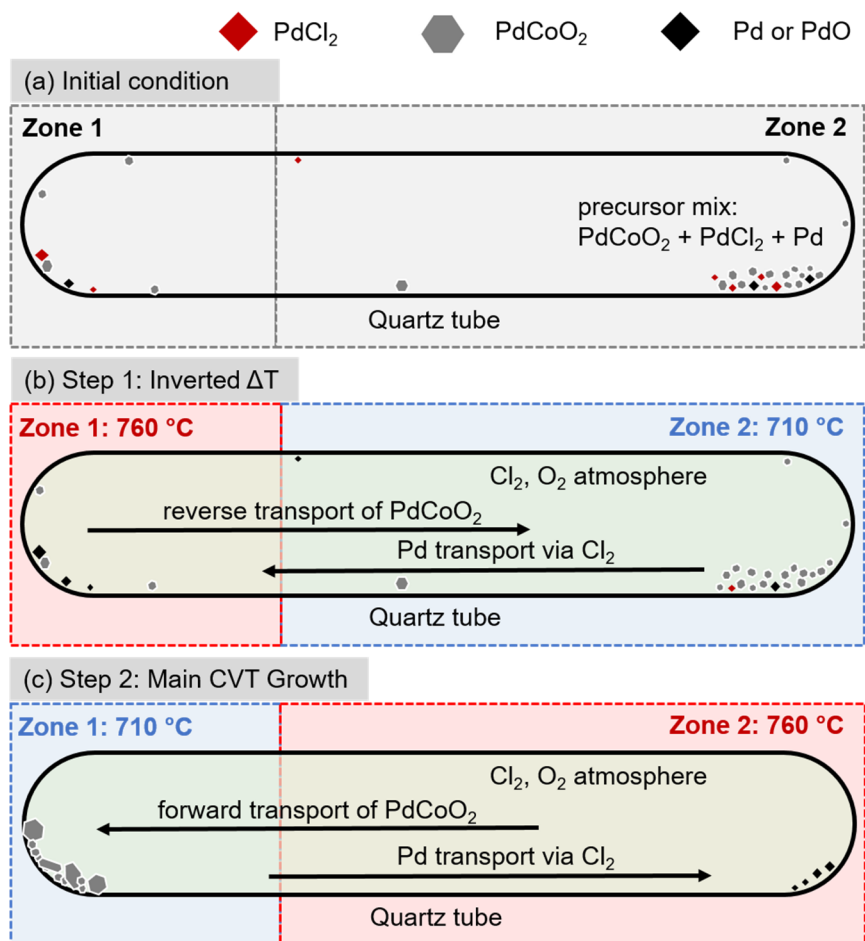


**Fig. S2. Schematics illustrating various stages of PdCoO<sub>2</sub> CVT growth.** Growth ampoules after (a) initial loading, (b) the first, inverted-temperature-gradient stage (3 days), and (c) the second, main growth stage (13 days). The legend at the top identifies PdCl<sub>2</sub>, PdCoO<sub>2</sub>, and Pd/PdO. In (a), the majority of the precursors (PdCoO<sub>2</sub> and PdCl<sub>2</sub> powder) are in Zone 2 but stray powder inevitably populates Zone 1. Pd is present only as an impurity in the metathesis/flux-grown PdCoO<sub>2</sub>. In (b), during the inverted-temperature-gradient stage, Zone 1 is at 760 °C and Zone 2 is at 710 °C. The PdCl<sub>2</sub> has partially decomposed into Pd and Cl<sub>2</sub>, and Cl<sub>2</sub> in turn reacts with PdCoO<sub>2</sub> to form PdCl<sub>2</sub>, CoCl<sub>2</sub>, and O<sub>2</sub>. PdCoO<sub>2</sub> is transported from Zone 1 to 2 (removing stray nuclei) but microscopic amounts of Pd (and possibly PdO) are transported from Zone 2 to 1. In (c), during the main growth stage, Zone 1 is at 710 °C and Zone 2 is at 760 °C. PdCoO<sub>2</sub> is transported from Zone 2 to Zone 1 and Pd is transported from Zone 1 to Zone 2.

## Section B. Specific Growth Parameters of Characterized Crystals

Tables S1 and S2 summarize the metathesis/flux and CVT growth conditions used to grow the specific PdCoO<sub>2</sub> crystals characterized in this paper. Powder X-ray diffraction (PXRD) was performed on almost all metathesis/flux and CVT crystals, and the other characterization/measurement techniques applied are listed in each case.

In addition to the characterization in the main text, Fig. S3 shows additional PXRD from four further metathesis/flux crystal batches and four further CVT batches. The phase purity is seen to significantly improve *via* CVT. As shown in Fig. S3(a), Co<sub>3</sub>O<sub>4</sub> and Pd minor phase impurities were commonly found in our metathesis/flux crystals. In CVT crystals (Fig. S3(b)), only a minor Pd phase impurity was ever detected.

**Table S1. Growth parameters of metathesis/flux-grown crystals.** Crystal growth parameters of metathesis/flux growth batches that produced samples characterized in this paper. Each batch corresponds to one ampoule. Listed are the batch numbers, growth temperature ( $T_{\text{growth}}$ ), dwell time at  $T_{\text{growth}}$ , cooling rate, and characterization methods. Characterizations that appear in the main text are bolded with the corresponding figure/table in parentheses. PXRD is powder X-ray diffraction, SEM is scanning electron microscopy, and ICP-MS is inductively coupled plasma mass spectrometry.

| <b>Batch number</b> | $T_{\text{growth}}$ (°C) | Dwell time at $T_{\text{growth}}$ (h) | Cooling rate (°C/h) | <b>Characterized by:</b>                                    |
|---------------------|--------------------------|---------------------------------------|---------------------|---|
| M/F06               | 700                      | 40                                    | 60                  | PXRD, <b>SEM</b> (Fig. 1(b)), <b>magnetometry</b> (Table 1) |
| M/F62               | 750                      | 150                                   | 40                  | PXRD, <b>optical imaging</b> (Fig. 1(b), inset)             |
| M/F29               | 750                      | 60                                    | 40                  | <b>PXRD</b> (Fig. 1(d))                                     |
| M/F30               | 750                      | 60                                    | 40                  | <b>PXRD</b> (Fig. 1(d))                                     |
| M/F55               | 750                      | 100                                   | 40                  | PXRD, <b>ICP-MS</b> (Table 2)                               |
| M/F56               | 750                      | 100                                   | 40                  | PXRD, <b>ICP-MS</b> (Table 2)                               |
| M/F59               | 750                      | 150                                   | 40                  | PXRD, <b>ICP-MS</b> (Table 2)                               |

**Table S2. Growth parameters of CVT-grown crystals.** Crystal growth parameters of CVT batches that produced samples characterized in this paper. Each batch corresponds to one ampoule. Listed are the batch numbers, cold and hot zone temperatures ( $T_{\text{cold}}$  and  $T_{\text{hot}}$ ), and characterization methods. Characterizations that appear in the main text are bolded with the corresponding figure/table in parentheses. PXRD is powder X-ray diffraction, ICP-MS is inductively coupled plasma mass spectrometry, PIXE is particle-induced X-ray emission, EDS is energy-dispersive X-ray spectroscopy, HRXRD is high-resolution X-ray diffraction, and RC is X-ray rocking curve analysis.

| <b>Batch number</b> | $T_{\text{cold}}$<br>(°C) | $T_{\text{hot}}$<br>(°C) | <b>Characterized by:</b>   |
|---------------------|---------------------------|--------------------------|--|
| CVT34               | 710                       | 760                      | PXRD, <b>optical imaging</b> (Fig. 1(c) inset), <b>ICP-MS</b> (Fig. 4(c), Table 2)                                       |
| CVT14               | 710                       | 760                      | PXRD, <b>optical imaging</b> (Fig. 1(c)), <b>PIXE</b> (Fig. 2(e))  |
| CVT12               | 710                       | 760                      | <b>PXRD</b> (Fig. 1(e)), optical imaging, <b>EDS</b> (Fig. 2(d)), transport  |
| CVT29               | 750                       | 800                      | PXRD, optical imaging, <b>Laue</b> (Fig. 2(a)), <b>HRXRD</b> (Fig. 2(c)), <b>RC</b> (Fig. 2(c) inset)                    |
| CVT24               | 710                       | 760                      | PXRD, optical imaging, <b>PIXE</b> (Fig. 2(e)), <b>ICP-MS</b> (Fig. 4(c), Table 2), magnetometry                         |
| CVT25               | 710                       | 760                      | PXRD, optical imaging, <b>PIXE</b> (Fig. 2(e)), <b>ICP-MS</b> (Fig. 4(c), Table 2), <b>transport</b> (Figs. 3(a,b)), VSM |
| CVT01               | 680                       | 740                      | PXRD, calorimetry, <b>magnetometry</b> (Fig. 3(c) and 3(d), Table 1), EDS  |
| CVT33               | 710                       | 760                      | PXRD, <b>ICP-MS</b> (Fig. 4(c), Table 2), PIXE   |

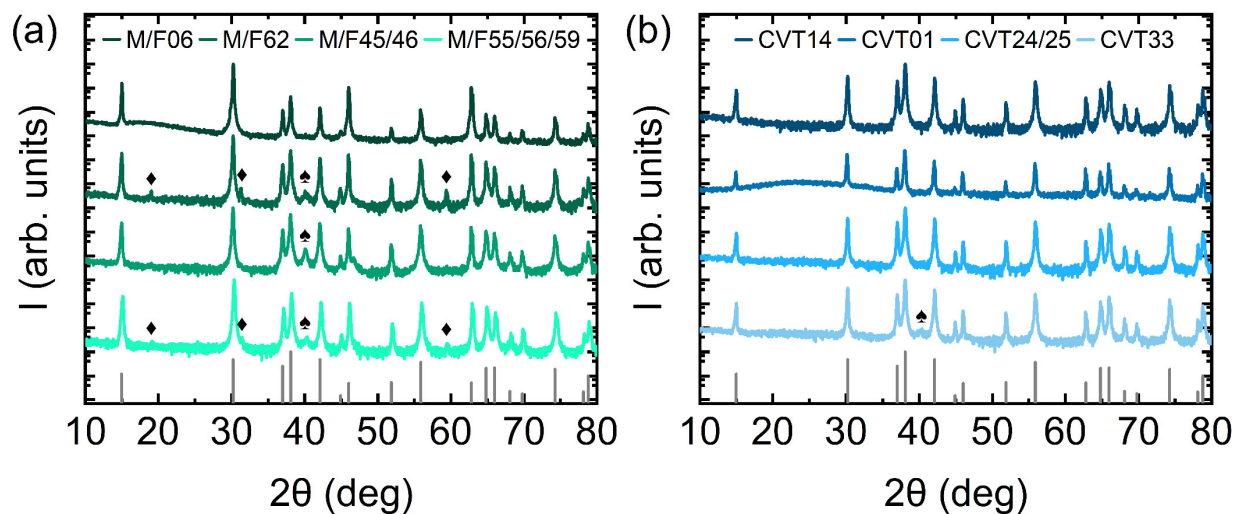


**Fig. S3. Additional PXRD data from metathesis/flux and CVT crystals.** PXRD scans (intensity  $I$  vs. angle  $2\theta$ ) from (a) four metathesis/flux crystal batches (green) and (b) four CVT crystal batches (blue). Peaks due to  $\text{Co}_3\text{O}_4$  and Pd phase impurities are marked with diamond and spade symbols, respectively.  $\text{PdCoO}_2$  reference patterns are shown at the bottom in gray (6, 74).

### Section C. Transport Measurement Details

**Offset Correction and Signal-to-noise Ratio.** As noted in the main text, the very low residual value of the  $a$ - $b$  plane resistivity ( $\rho_{ab}$ ) in PdCoO<sub>2</sub> single crystals renders low-temperature ( $T$ ) transport measurements challenging. Specifically, signal-to-noise ratio becomes an issue, as do instrumental offsets. These issues were alleviated in this work through the study of relatively long bar-shaped crystals (Fig. 3(a), inset), but must still be carefully addressed. The signal-to-noise ratio was maximized through the use of an AC resistance bridge (a Lakeshore 370 operating at 13.7 Hz) in tandem with a preamplifier/channel scanner (a Lakeshore 3708). Currents of 10 mA were employed and self-heating was rigorously ruled out by estimations of the (very low) deposited power, and careful low- $T$  checks of resistance *vs.* current and resistance *vs.*  $T$  at various excitation currents. The resulting noise performance is illustrated below and in the data of Figs. 3(a,b).

With respect to offsets, which are critical given the  $\sim 20 \mu\Omega$  residual resistances, these were first carefully characterized *via* parallel measurements of zero-resistance superconducting V thin films. The latter were Si/Si-N/V(100 nm) films deposited in ultrahigh vacuum in a molecular beam epitaxy system. As shown in the inset to Fig. S4, the same top-contact, in-line, four-wire geometry as was used for PdCoO<sub>2</sub> crystals (Fig. 3(a), inset) was employed for the V films. The four contacts are labeled A, B, C, D, and a standard notation for four-wire resistance ( $R$ ) measurements is followed by using the first two letters to refer to the  $I^+$  and  $I^-$  terminals, respectively, and the last two letters to refer to the  $V^+$  and  $V^-$  terminals, respectively, *e.g.*,  $R_{ADBC}$ . As shown in Fig. S4, the nominally zero-magnetic-field  $R_{ADBC}(T)$  of such films reveals a superconducting transition with an onset temperature of  $\sim 5.2$  K and an endpoint of  $\sim 5.1$  K, in agreement with expectations (79). Such samples were thus measured at 3.9 K, safely in the zero-resistance regime, to characterize the voltage and resistance offsets in our measurement set-up.

Offset measurements were made both with and without the preamplifying channel scanner. Table S3 shows typical results for two separate sets of contacts on V films at 3.9 K. The first three data columns are without the preamplifier, and the last three data columns are with the preamplifier. Considering the data without the preamplifier first, measurements of  $R_{ADBC}$  and  $R_{DACB}$  were found to be near identical, at  $-0.4$  to  $-0.3 \mu\Omega$  for Contact Set 1 and  $0.3$  to  $0.7 \mu\Omega$  for Contact Set 2. Such findings are representative. Over many measurements, using different wire and contact sets, different bridge ranges and currents (10 mA was used in Table S3), *etc.*, the resistances offsets

from zero were found to be approximately  $\pm 1 \mu\Omega$ , with noise of approximately  $\pm 0.5 \mu\Omega$ . Most importantly, the approximately  $\pm 1 \mu\Omega$  offset indicates that measurements of  $\sim 20 \mu\Omega$  resistance can be made with reasonable accuracy. Adding the preamplifier to the set-up (right side of Table S3) was found to result in differences. The noise dropped to approximately  $\pm 0.1 \mu\Omega$  (by roughly a factor of 5), but the offsets from zero resistance were found to grow to approximately  $\pm 5 \mu\Omega$  (also by roughly a factor of 5). Interestingly, however, it was found empirically that the sign of the offset reproducibly inverted on going from  $R_{ADBC}$  to  $R_{DACB}$ , *i.e.*, with a  $180^\circ$  phase shift of the excitation (Table S3). Averaging between  $R_{ADBC}$  and  $R_{DACB}$  thus yielded offsets of only  $\pm 1-2 \mu\Omega$ , over many measurements, using different wire and contact sets, different bridge ranges and currents, *etc.* Thus, regardless of whether the preamplifier was included, offsets from zero resistance could be kept to a workable  $\pm 1-2 \mu\Omega$ .

Based on the above characterization of offsets in the measurement setup, PdCoO<sub>2</sub> single-crystal measurements were made two ways. First, for the residual resistance measurement at  $\sim 4$  K on the CVT-grown PdCoO<sub>2</sub> crystal in the inset to Fig. 3(a), the preamplifier was removed, resulting in  $R_{ADBC} = 19.4 \mu\Omega$  as the average value, with a noise level of approximately  $\pm 0.5 \mu\Omega$ . Accepting the  $\pm 1 \mu\Omega$  offset from the above analysis, using the measured sample dimensions ( $0.0225 \pm 0.0006$  mm thick,  $1.045 \pm 0.005$  mm long, and  $0.20 \pm 0.02$  mm wide), and propagating errors then leads to a residual  $\rho_{ab}$  of  $8 \pm 1$  n $\Omega$  cm. Combining this with the measured 300-K  $R_{ADBC}$  of  $8465 \pm 5 \mu\Omega$  (where the offset is negligible) yields the RRR of  $436 \pm 25$  quoted in the main text. Second, for low-noise  $\rho_{ab}(T)$  measurements (see Figs. 3(a,b)), the preamplifier was inserted and both  $R_{ADBC}(T)$  and  $R_{DACB}(T)$  were measured, as shown in Fig. S5. Based on the above analysis, these values were then averaged to the solid line in Fig. S5, thereby accounting for the offsets to within  $\pm 1-2 \mu\Omega$ .

***Finite-element Simulations of Current Flow and Voltage Drop.*** As noted in the main text, the large *c*-axis/*a*-*b*-plane resistivity ratio ( $\rho_c/\rho_{ab}$ ) of PdCoO<sub>2</sub> single crystals (5, 8, 14–16) provides a second measurement challenge. Specifically, the top-contact geometry used here, while convenient, must lead to some level of additional systematic error due to some inevitable current flow along *c*-axis directions. Finite element current flow and voltage drop simulations were thus performed using COMSOL Multiphysics. For these simulations, samples with dimensions close to the crystal in Fig. 3(a) were set up, as shown in Fig. S6. Two current injection geometries were studied. Fig. S6(a) shows the top-contact geometry employed in our experiments, while Fig. S6(b)

shows a side-contact geometry for current injection. The former closely replicates the experimental geometry, while the latter illustrates the effect of more ideally constraining the current in the  $a$ - $b$ -plane, thus minimizing the influence of the large  $\rho_c/\rho_{ab}$ . The boundary conditions applied in both geometries consisted of a 10 mA current flow from contact A, with a grounded contact D; an automatically generated mesh was used in the simulations.

For the purposes of initial illustration, Figs. S6(a,b) are simulation results based on the reported  $\rho_{ab}$  (17) and  $\rho_c$  (14) of metathesis/flux-grown single crystals (with RRR = 376), the  $\rho_{ab}$  values being from ion-beam-patterned crystals (17). Although it impacts the results negligibly, the contacts were simulated using typical resistivities for Cu. All of the 300-K and low- $T$  resistivity values are listed in Table S4. As shown by Fig. S6(b), using 300-K values, the color maps of voltage drop in the side-current-contact geometry are as expected. No potential differences are apparent between the top and bottom of the crystal, and the voltage is dropped gradually from A to D. As shown by Fig. S6(a), however, this is not so when the all-top-contact geometry is simulated. Due to the large  $\rho_c/\rho_{ab}$ , distinct ( $\sim 25\%$ ) potential differences arise from the top to the bottom of the crystal near the contacts, despite the thickness of only 22  $\mu\text{m}$ . For quantification, the simulation results were then used to determine the 4-terminal resistance using  $R = (V_C - V_B)/I$ . The results are summarized in Table S4 (right columns) for the side-contact and top-contact geometries. The side-contact results are as expected, reproducing the input RRR from resistivity to good accuracy. The top-contact simulated  $R$  values are 50-90% larger than those for side current contacts, however, due to the effect of the large  $\rho_c/\rho_{ab}$ . This effect worsens with decreasing  $T$  as  $\rho_c/\rho_{ab}$  grows on cooling (also shown in Table S4). The top-contact RRR of 278 is thus  $\sim 20\%$  smaller than the side-contact (true) value. As stated in the main text, measured RRR values in this work ( $\sim 440$  for CVT crystals) are thus lower bounds due to overestimation of the residual  $\rho_{ab}$ .

Further quantification of the extent of underestimation of the RRR was achieved by running additional top-contact simulations that reproduce the observed RRR of  $\sim 440$ . This was done by finding the required true value of residual  $\rho_{ab}$  to reproduce the experimental results, while keeping the 300-K value of  $\rho_{ab}$  (which is dominated by phonon, not impurity, scattering) constant. (In the absence of additional information,  $\rho_c$  was also maintained at the same values as in prior simulations). As shown in Table S5, the true residual  $\rho_{ab}$  required to reproduce a top-current-contact RRR of 436 is 4.4 n $\Omega\text{cm}$ , close to half the measured value. The measured RRR of 436, by

our best estimates, thus corresponds to a true value of 670 (Table S5). As noted in the main text, these estimates are further supported by unitary scattering limit calculations, which indicate that our measured Pd-plane impurity density is consistent with this residual  $\rho_{ab}$  to within 15-30%. Note that the above simulations assume  $\rho_c$  is unchanged from metathesis/flux crystals to CVT crystals. If we were to assume some reduction in  $\rho_c$ , which is likely based on the higher purity, then the  $\rho_{ab}$  needed to reproduce the measured top-contact RRR would increase. The RRR estimate of 670 should thus be viewed as an upper bound for the true value, yielding  $440 < \text{RRR} < 670$ .

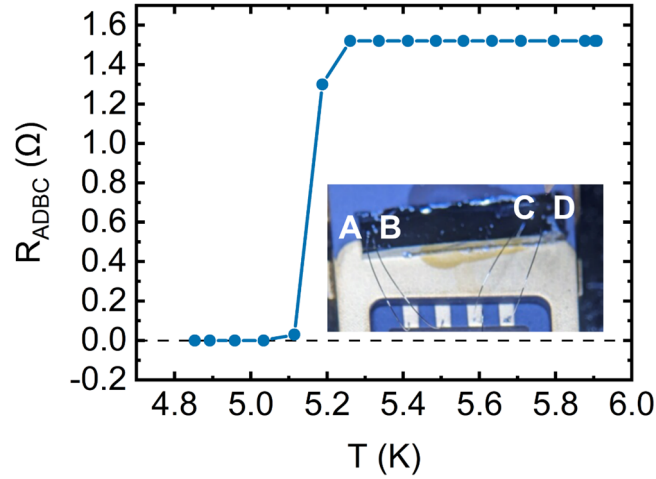


**Fig. S4. Superconducting transition of V thin films used for offset characterization.**  $R_{ADBC}(T)$  (see above text for definition) of a Si/Si-N/V(100 nm) film. Note the onset and endpoints of the superconducting transition at approximately 5.2 and 5.1 K, respectively. Inset: Optical image of the substrate/film mounted on a chip package. The wire-bonded Al contacts are labeled A, B, C, D. Current was driven A-D, while the voltage drop was measured B-C.

**Table S3. Offset characterization via 3.9 K measurements of superconducting V thin films.**

Various measured 3.9-K resistances of Si/Si-N/V(100 nm) films. The results shown are averaged over 10-60 measurements, on two contact sets; the uncertainties listed are resulting standard deviations. The excitation current was 10 mA. Shown are  $R_{ADBC}$ ,  $R_{DACB}$  and their average (see text above for definitions), both without (left) and with (right) the preamplifying channel scanner.

|                | $R_{ADBC}$ ,<br>w/o preamp<br>( $\mu\Omega$ ) | $R_{DACB}$ ,<br>w/o preamp<br>( $\mu\Omega$ ) | $R_{average}$ ,<br>w/o preamp<br>( $\mu\Omega$ ) | $R_{ADBC}$ ,<br>w/ preamp<br>( $\mu\Omega$ ) | $R_{DACB}$ ,<br>w/ preamp<br>( $\mu\Omega$ ) | $R_{average}$ ,<br>w/ preamp<br>( $\mu\Omega$ ) |
|----------------|---|---|--|--|--|---|
| Contact Set #1 | $-0.4 \pm 0.6$                                | $-0.3 \pm 0.6$                                | $-0.4 \pm 0.4$                                   | $5.6 \pm 0.2$                                | $-4.1 \pm 0.3$                               | $0.8 \pm 0.2$                                   |
| Contact Set #2 | $0.3 \pm 0.5$                                 | $0.7 \pm 0.6$                                 | $0.5 \pm 0.4$                                    | $6.1 \pm 0.1$                                | $-5.63 \pm 0.05$                             | $0.24 \pm 0.06$                                 |

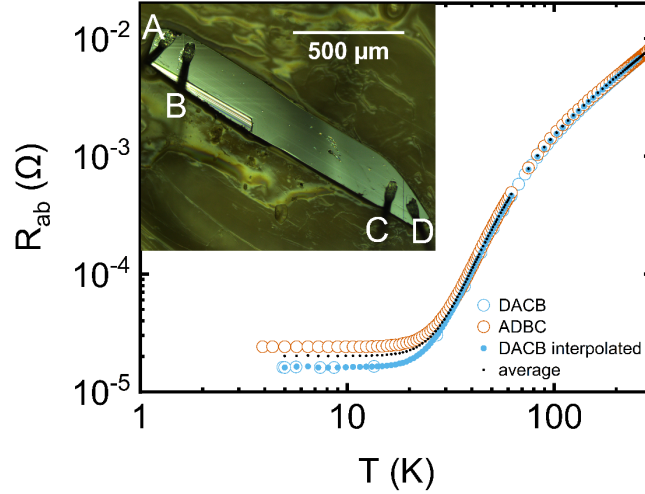


**Fig. S5. Offset correction of  $\text{PdCoO}_2$   $\rho_{ab}(T)$  measurements.**  $R_{ADBC}$  and  $R_{DACB}$  vs.  $T$  for the CVT-grown crystal in Figs. 3(a,b). The measurements were made with 10 mA excitation with the preamplifying channel scanner. After interpolation of  $R_{DACB}(T)$  to generate data at identical temperatures to  $R_{ADBC}(T)$ , the two data sets were averaged (see the above text for detailed justification), resulting in the black data points, upon which Figs. 3(a,b) are based.

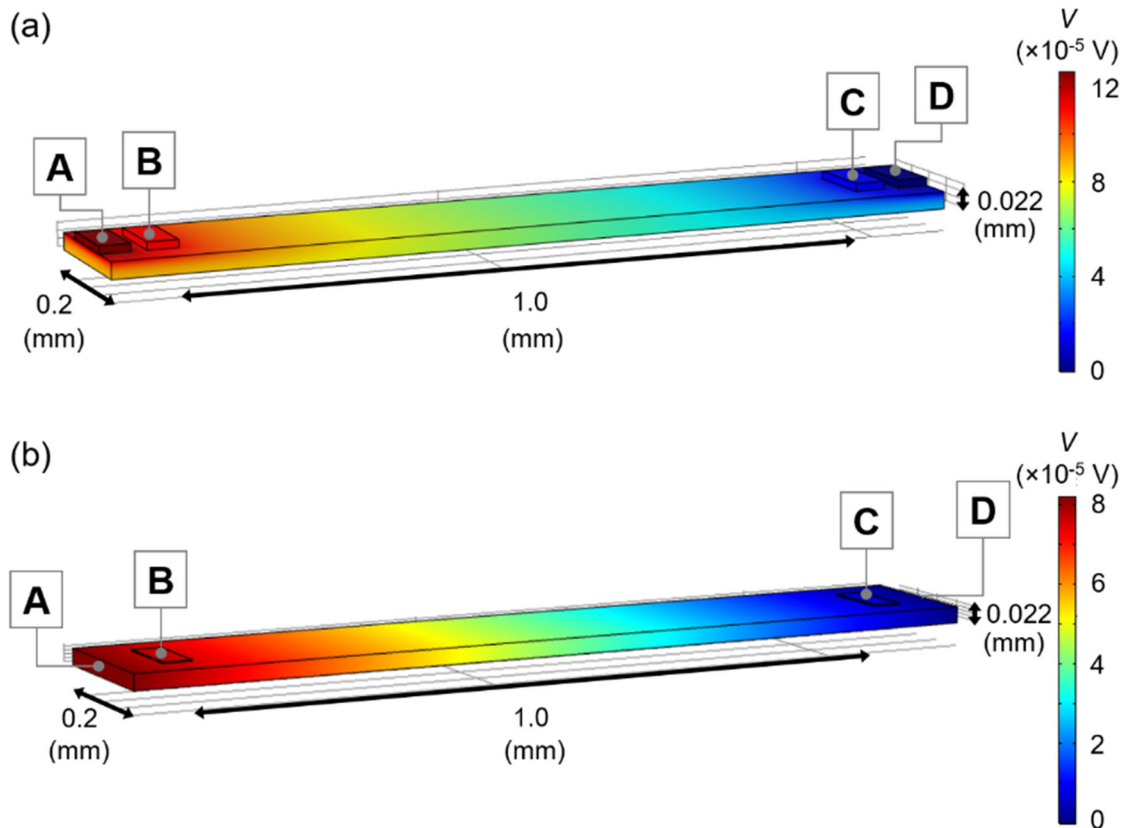


**Fig. S6. Finite element simulations of current flow and voltage drop in PdCoO<sub>2</sub> crystals.** Simulations were performed with COMSOL Multiphysics on crystals with dimensions ( $0.022 \times 1.000 \times 0.200 \text{ mm}^3$ ), designed to closely resemble the crystal in Figs. 3(a,b). Panel (a) is for a geometry with all top contacts, while (b) is for a geometry with side current contacts. The contacts are labeled A, B, C, D, an excitation current of 10 mA was used (injected at A and extracted at D), and the relevant resistivity parameters are discussed in the text and shown in Table S4. Contacts B and C are the voltage contacts, placed 1 mm apart, edge-to-edge. The resulting simulated 300-K voltage drops are shown as color maps based on the scale to the right. Note the through-thickness color gradient near the contacts in (a).

**Table S4. Input resistivity values and extracted resistances from finite element simulations.**

Shown are 300-K and residual low- $T$  values of the PdCoO<sub>2</sub>  $a$ - $b$  plane resistivity,  $c$ -axis resistivity, their ratio, and the Cu contact resistivity (14, 17, 80), which were used as inputs for the simulations. As described above, the PdCoO<sub>2</sub> values shown are from metathesis/flux-grown crystals (14, 17), measured on focused-ion-beam patterned samples for the  $a$ - $b$ -plane case (17). The last two columns show the output from such simulations, specifically the simulated four-wire resistance ( $R_{\text{sim}}$ ) in the top-current-contact and side-current-contact geometries. Corresponding PdCoO<sub>2</sub> RRR values are shown in the bottom row.

|          | $\rho_{ab}$<br>( $\Omega$ cm) | $\rho_c$<br>( $\Omega$ cm) | $\rho_c/\rho_{ab}$ | $\rho_{Cu}$<br>( $\Omega$ cm) | $R_{\text{sim, top contact}}$<br>(m $\Omega$ ) | $R_{\text{sim, side contact}}$<br>(m $\Omega$ ) |
|----------|-------------------------------|----------------------------|--------------------|-------------------------------|--|---|
| 300 K    | $3.05 \times 10^{-6}$         | $1.03 \times 10^{-3}$      | 338                | $1.67 \times 10^{-6}$         | 10.2   | 7.03  |
| Low- $T$ | $8.1 \times 10^{-9}$          | $6.0 \times 10^{-6}$       | 741                | $7 \times 10^{-12}$           | 0.0367   | 0.0193  |
| RRR      | 376                           | 171                        |                    |                               | 278  | 364   |

**Table S5. Simulation parameters reproducing the observed RRR ratio in top-contact measurements.** Shown are analogous parameters to Table S4, with the exception that the input low- $T$  (residual) value of  $\rho_{ab}$  (bolded) has been selected to reproduce the measured top-contact RRR of  $\sim 440$ . The deduced residual  $\rho_{ab}$  of  $4.44 \text{ n}\Omega \text{ cm}$  generates a top-contact RRR of 436, which the simulations suggest requires a side-current-contact (true) RRR of 670 (rightmost column).

|          | $\rho_{ab}$<br>( $\Omega \text{ cm}$ )  | $\rho_c$<br>( $\Omega \text{ cm}$ ) | $\rho_c/\rho_{ab}$ | $\rho_{Cu}$<br>( $\Omega \text{ cm}$ ) | $R_{\text{sim, top contact}}$<br>( $\text{m}\Omega$ ) | $R_{\text{sim, side contact}}$<br>( $\text{m}\Omega$ ) |
|----------|---|-------------------------------------|--------------------|--|---|--|
| 300 K    | $3.05 \times 10^{-6}$                   | $1.03 \times 10^{-3}$               | 338                | $1.67 \times 10^{-6}$                  | 10.2  | 7.03   |
| Low- $T$ | <b><math>4.44 \times 10^{-9}</math></b> | $6.0 \times 10^{-6}$                | 1350               | $7 \times 10^{-12}$                    | 0.0234  | 0.0105   |
| RRR      | 687                                     | 171                                 |                    |  | 436   | 670  |

#### **Section D. ICP-MS Trace Impurity Analysis Details**

As noted in the main text, 54 elements were selected for ICP-MS trace impurity analysis of both metathesis/flux- and CVT-grown PdCoO<sub>2</sub> crystals. The selection of these 54 elements was based on their being either known to form ABO<sub>2</sub> compounds, or being known impurities in the growth reagents. A full listing of these elements, and their corresponding analyte and analysis mode is provided in Table S6. Elements that are known to form at least one ABO<sub>2</sub> compound were first identified, in part using Ref. (24). Purity certifications for the commercial reagents used in the crystal growth processes were then examined. Table S7 shows the grades and predominant impurities of the reagents used in most crystal growth batches in this work, including the crystals that were used for ICP-MS and transport measurements. The least pure reagent, Pd, is >99.995% pure, corresponding to <55 ppm impurities. Based on Table S7, the detected presence of Ni, Mn, Fe, Sn, Ir, and Ag in the final PdCoO<sub>2</sub> crystals (see Table 2) is thus expected at some level. Additionally, Pt would not be surprising as an impurity in a Pt-group reagent element such as Pd, and the presence of Ni, Mn, Fe, and Zn in the reagents suggests that the first-row transition metals Cu and Cr would also not be unexpected. All the elements in the middle and bottom panels of Table 2 can thus be reasonably accounted for based on the reagents, with the exception of Al. The latter may arise from Al-containing sample handling apparatus, particularly weighing boats.

**Table S6. Tested elements and ICP-MS analytical conditions**

Analytical conditions for all the trace elements quantified in this work by ICP-MS. The analyte for each element is listed in the second column, with the corresponding analysis mode in the third column. Kinetic energy discrimination helium collision cell (KED-He) or triple quadrupole oxygen collision cell (TQ-O<sub>2</sub>) mode were used.

| Element | Analyte                           | Analysis mode     | Element | Analyte                            | Analysis mode     |
|---------|-----------------------------------|-------------------|---------|------------------------------------|-------------------|
| Li      | <sup>7</sup> Li                   | KED-He            | Pd      | <sup>105</sup> Pd                  | TQ-O <sub>2</sub> |
| B       | <sup>11</sup> B                   | KED-He            | Ag      | <sup>107</sup> Ag                  | TQ-O <sub>2</sub> |
| Na      | <sup>23</sup> Na                  | KED-He            | In      | <sup>115</sup> In                  | KED-He            |
| Mg      | <sup>24</sup> Mg                  | KED-He            | Sn      | <sup>118</sup> Sn                  | KED-He            |
| Al      | <sup>27</sup> Al                  | KED-He            | Ba      | <sup>138</sup> Ba                  | KED-He            |
| Si      | <sup>29</sup> Si                  | KED-He            | La      | <sup>139</sup> La                  | TQ-O <sub>2</sub> |
| K       | <sup>39</sup> K                   | KED-He            | Ce      | <sup>140</sup> Ce. <sup>16</sup> O | TQ-O <sub>2</sub> |
| Ca      | <sup>44</sup> Ca                  | KED-He            | Pr      | <sup>141</sup> Pr. <sup>16</sup> O | TQ-O <sub>2</sub> |
| Sc      | <sup>45</sup> Sc. <sup>16</sup> O | TQ-O <sub>2</sub> | Nd      | <sup>144</sup> Nd. <sup>16</sup> O | TQ-O <sub>2</sub> |
| Ti      | <sup>49</sup> Ti                  | KED-He            | Sm      | <sup>149</sup> Sm. <sup>16</sup> O | TQ-O <sub>2</sub> |
| V       | <sup>51</sup> V. <sup>16</sup> O  | TQ-O <sub>2</sub> | Eu      | <sup>153</sup> Eu                  | TQ-O <sub>2</sub> |
| Cr      | <sup>52</sup> Cr. <sup>16</sup> O | TQ-O <sub>2</sub> | Gd      | <sup>157</sup> Gd. <sup>16</sup> O | TQ-O <sub>2</sub> |
| Mn      | <sup>55</sup> Mn                  | KED-He            | Tb      | <sup>159</sup> Tb. <sup>16</sup> O | TQ-O <sub>2</sub> |
| Fe      | <sup>57</sup> Fe                  | KED-He            | Dy      | <sup>163</sup> Dy. <sup>16</sup> O | TQ-O <sub>2</sub> |
| Co      | <sup>59</sup> Co                  | TQ-O <sub>2</sub> | Ho      | <sup>165</sup> Ho. <sup>16</sup> O | TQ-O <sub>2</sub> |
| Ni      | <sup>60</sup> Ni                  | KED-He            | Er      | <sup>166</sup> Er. <sup>16</sup> O | TQ-O <sub>2</sub> |
| Cu      | <sup>63</sup> Cu                  | KED-He            | Tm      | <sup>169</sup> Tm. <sup>16</sup> O | TQ-O <sub>2</sub> |
| Zn      | <sup>66</sup> Zn                  | KED-He            | Yb      | <sup>172</sup> Yb                  | TQ-O <sub>2</sub> |
| Ga      | <sup>71</sup> Ga                  | KED-He            | Lu      | <sup>175</sup> Lu. <sup>16</sup> O | TQ-O <sub>2</sub> |
| As      | <sup>75</sup> As. <sup>16</sup> O | TQ-O <sub>2</sub> | W       | <sup>182</sup> W                   | KED-He            |
| Rb      | <sup>85</sup> Rb                  | KED-He            | Re      | <sup>185</sup> Re                  | KED-He            |
| Sr      | <sup>88</sup> Sr. <sup>16</sup> O | TQ-O <sub>2</sub> | Os      | <sup>189</sup> Os                  | KED-He            |
| Y       | <sup>89</sup> Y. <sup>16</sup> O  | TQ-O <sub>2</sub> | Ir      | <sup>193</sup> Ir                  | TQ-O <sub>2</sub> |
| Zr      | <sup>90</sup> Zr. <sup>16</sup> O | TQ-O <sub>2</sub> | Pt      | <sup>195</sup> Pt                  | TQ-O <sub>2</sub> |
| Mo      | <sup>98</sup> Mo. <sup>16</sup> O | TQ-O <sub>2</sub> | Au      | <sup>197</sup> Au                  | TQ-O <sub>2</sub> |
| Ru      | <sup>101</sup> Ru                 | TQ-O <sub>2</sub> | Hg      | <sup>202</sup> Hg                  | TQ-O <sub>2</sub> |
| Rh      | <sup>103</sup> Rh                 | TQ-O <sub>2</sub> | Tl      | <sup>205</sup> Tl                  | KED-He            |

**Table S7. Reagent grades and impurities**

Purity grades and predominant impurity elements (> 1 ppm) from the manufacturers' certificates of analyses for the commercial reagents used to grow the crystals characterized here by ICP-MS.

|                                | <b>Manufacturer</b>      | <b>Reagent grade</b> | <b>Predominant impurity elements found</b> |
|--------------------------------|--------------------------|----------------------|--|
| Co <sub>3</sub> O <sub>4</sub> | Alfa Aesar               | 99.9985% (≤ 15 µg/g) | Fe, Mn, Ni, Ca, Zr, Mg, Zn                 |
| PdCl <sub>2</sub>              | Thermo Fisher Scientific | 99.999% (≤ 10 µg/g)  | Rh   |
| Pd                             | Sigma-Aldrich            | 99.995% (≤ 55 µg/g)  | Ag, Fe, Ca, Sn, As, Ir, K, Mo              |